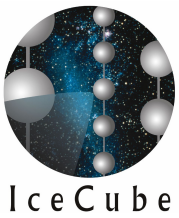

UNIVERSITÉ DE MONS

FACULTÉ DES SCIENCES

Combined Search for Neutrinos from Dark Matter Annihilation in the Galactic Centre using IceCube and ANTARES

Author:
Nadège Iovine

Thesis supervisor:
Juan Antonio Aguilar Sánchez
Evelyne Daubie

Département de Physique
Service de Physique des Particules Elémentaires

Academic year 2016-2017

UMONS
Université de Mons

Faculté
des Sciences

Contents

Chapter 1

Introduction

As soon as in the 30s, astronomical observation provided evidences of "unseen matter", the so-called dark matter (DM). But, even if we have strong proof of its existence, the nature of dark matter remains unknown. Multiple theories have been proposed, including a modification of the Newton's laws called Modified Newtonian Dynamic (MoND). To date, the most commonly admitted hypothesis is that dark matter is made out of particles, unobserved yet, called Weakly Interactive Massive Particles (WIMPs). WIMPs are supposed to be non-baryonic particles that are non-relativistic, electromagnetically neutral and interacting only via weak interactions. In the following, we consider dark matter to be composed of WIMPs. Various WIMP masses and annihilation channels are exposed in this work.

While we still don't know what compose dark matter, it's distribution in the Universe is continuously improving. According to observation, galaxies are surrounded by a dark matter halo. Numerous halo model have been proposed in order to match the observation. According to these models, dark matter have a high density in the centre of the galaxy. Our galaxy being no exception, looking for dark matter annihilation products from the Galactic Centre seems a reasonable idea.

Several approaches are used in order to search for DM particles. All these experiments can be expressed in three main categories : direct searches, DM production in particles accelerator and indirect searches. Our analysis consists of an indirect search for dark matter annihilation in the Galactic Centre using IceCube and ANTARES. Indirect search experiments are looking for secondary particles produced in the decay or annihilation of DM. Most candidates for DM particles annihilates by pair, giving us particles of the Standard Model (SM), with among them neutrinos.

Upon non-dection, the purpose of such searches is to measure the thermal average self-annihilation cross-section of dark matter, $\langle \sigma_A \nu \rangle$. Upon non-detecion, an upper limit on $\langle \sigma_A \nu \rangle$ can be set for each of the WIMP masses considered. Limits on WIMP dark matter annihilation cross-section have already been set by neutrino detectors such as IceCube [13] and ANTARES [**ANTARES**].

IceCube and ANTARES are neutrino telescopes located respectively in the South Pole ice and deep Mediterranean sea. Both detectors follow the same detection principle, using the Cherenkov radiation produced by the secondary particles. Due to the small interaction cross section of neutrinos, a large volume of target material is needed. This is done by using a sparse array of photomultiplier tubes in a large volume of dielectric medium, respectively ice and sea water. The photodectors will record the hits due to Cherenkov photons. The reconstruction of the event will then be performed

using specific algorithm.

This master thesis is divided in nine chapters, the first being the introduction. Throughout the first chapters, all the important concepts will be introduced. In chapter 2, the main evidences of dark matter are exposed, as well as the most common hypotheses of what it could consist of. A brief reminder on neutrinos and their interaction with matter can be found in chapter 3. The detection principle and detectors configuration are discussed in chapter 4. Furthermore, the expected background for indirect WIMP searches with neutrino telescope is also explained in this chapter. The following parts of this master thesis focus on the analysis method, starting with the data selection done over the IceCube and ANTARES samples, which can be found in chapter **??** and **??** respectively. The statistical concepts needed for our analysis are exposed in chapter 6, along with the Feldman-Cousins Method. This chapter is also dedicated to the analysis method and the results we obtained. Finally, the conclusion outlines the final results and the future steps of the combined analysis.

Chapter 2

Dark matter

The need to postulate the existence of Dark Matter was proposed for the first time by Fritz Zwicky in the 30s. By using the Virial theorem, he observed that the galaxies in the Coma cluster had a higher speed than what was predicted from the luminous matter [**Zwicky**]. Ever since, various proposals have been made on what the dark matter could consist of. One of the possibilities is that dark matter stands under the form of non luminous astrophysical objects made out of the same matter as ordinary astrophysical objects such as stars. It could also be composed of new particles outside of the Standard Model of particle physics. According to the actual estimations, dark matter is more likely to be composed of non-baryonic matter. Indeed, ordinary matter, composed of quarks and leptons, seems to only account for 5% of the energy-density of the Universe. While, dark matter contribution to the energy density is of about 25% and the remaining part is attributed to dark energy (supposedly causing the accelerated expansion of the Universe).

2.1 Evidences of Dark Matter

The observation of rotation curves of spiral galaxies, i.e. rotation speed in regard to the radial distance of the objects, give us an indirect evidence of missing matter in the form of non-luminous matter. In the late 1960s, Vera Rubin and Kent Ford measured the rotation curves of high-luminosity spiral-galaxies, highlighting the fact that these rotation curves are approximately flat [9]. This observation implies that the galaxy mass increases significantly with the distance r to its centre.

Let us consider a star of mass m moving at a speed v and situated at a distance r of the Galactic Centre. Equalizing the gravitational equation and the centrifuge force, we get the following equation

$$\frac{mv^2}{r} = \frac{mM(r)G}{r^2} \,, \tag{2.1}$$

where $M(r)$ is the mass inside the radius r and G is the gravitational constant. For a spiral galaxy like the Milky Way, most of the luminous matter is concentrate in the hub. For a star inside the hub we expect $M(r) \propto r^3$ and therefore $v \propto r$; whereas outside of the hub, we foresee a behaviour of $M(r) \propto r$ and thus $v \propto r^{-1/2}$. Hence, the speed must decrease as the radius increase. Rather, observation tend to show that the speed is relatively steady for high r as seen in figure 2.1.

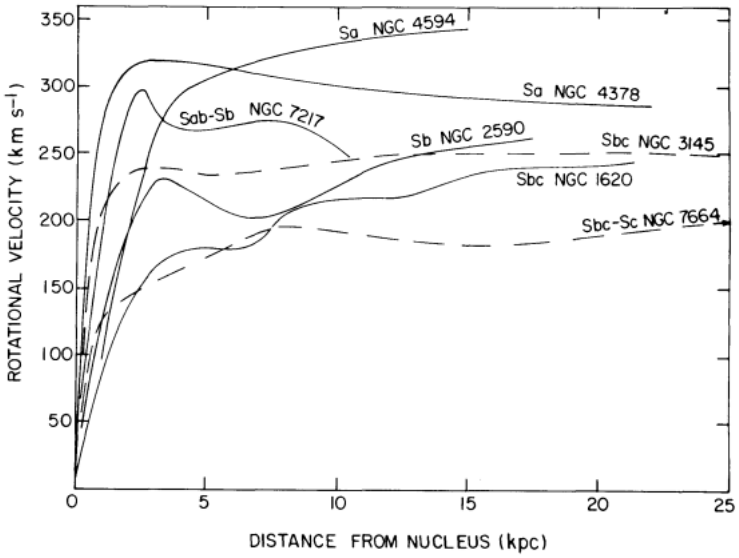

FIGURE 2.1: Rotation speed of seven spiral galaxies, in regards to the distance from the Galactic Centre taken from [9]

2.1.1 Gravitational Lensing

Gravitational lensing gives us crucial information concerning the amount and location of dark matter. Gravitational lensing is defined by the deviation of photons from distant sources by a distribution of matter, *i.e.* the lens, between the light sources and the observer. We can distinguish strong gravitational lensing from weak gravitational lensing. For strong gravitational lensing, the mass standing between the source and the observer is large enough to deform the image of the source to an arc. These arcs appear multiple times, forming a ring around the lens. Such rings are known as Einstein rings. On the contrary, for weak gravitational lensing, the lens is not massive enough to distort objects distinctly. Rather, a statistical analysis is performed on the distortion of many backgrounds sources to obtain the properties of the lens. Mass of galaxy clusters can be deduced from their gravitational lensing effects on more distant objects. The deflection angle α of a photon by a mass M at the distance of closest approach b is given by the following equation [**lensing**]

$$\alpha = \frac{4GM}{c^2 b} \, . \tag{2.2}$$

2.1.2 Evidence of Dark Matter from Gravitational Lensing

One of the most conclusive evidence of dark matter was given by the observation of the Bullet Cluster using a combination of observations from the Hubble Space Telescope, the ESO Very Large Telescope, the Magellan telescope and the Chandra satellite [**Bullet_cluster**]. The first hint of dark matter in the bullet cluster is the high mass to luminosity ratio, indicating a high proportion of dark matter in the galaxy cluster. Using the weak gravitational lensing effects on more distant galaxies, the gravitational potential in the cluster have been mapped. Meanwhile, the X-ray signals tell us more about the distribution of plasma in the galaxies clusters. As shown in fig. 2.2, the weak gravitational lensing reconstructions are located in two separated regions. Similarly,

the X-ray emission (and thus the plasma) seems to be located in two zones, nevertheless well segregated from the dark matter regions. If there was no presence of dark matter in the merging cluster 1E 0657-558, the plasma component would dominate the total mass of the cluster and thus, the reconstructed gravitational potential would be located around the X-ray emitting plasma. The importance of this observation is that we can see a separation of the dark matter and the baryonic matter. During the collision of two galaxy clusters, the gas cloud would be slowed due to electromagnetic interaction, while the dark matter, supposedly affected only via gravitational interaction, would not.

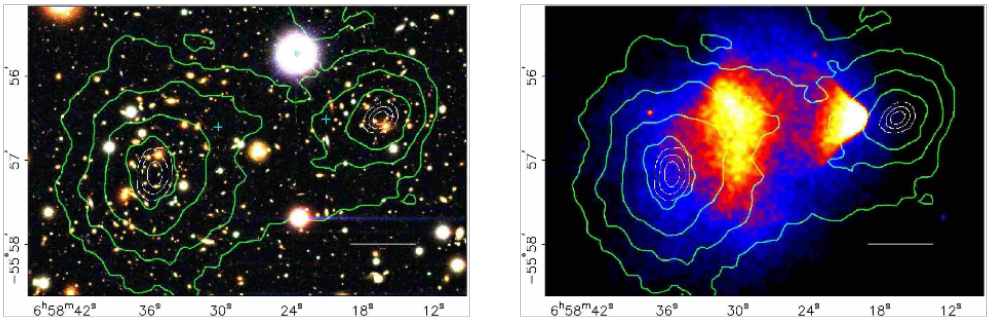

FIGURE 2.2: The merging cluster 1E 0657-558, or "Bullet Cluster", shown in optical spectrum (right) and X-Ray observation (left). The white bar indicating 200 kpc at the distance where stand the cluster. The green contours in both maps represent the weak gravitational lensing reconstruction. The white contours show the errors on the position of the gravitational peaks at 68.3%, 95.5%, and 99.7% confidence level. The blue crosses indicate the location of the centres used to measure masses of the X-ray emitting plasma clouds. Figure from [**bullet**].

2.2 Dark Matter Candidates

As mentioned previously, multiple hypothesis have been made in order to explain the observations of dark matter. Among them, three main categories stand out. The first category attempt to explain the unseen mass with the presence of non-luminous baryonic matter. The second category is postulating the existence of heavy new particles, beyond the standard model (BSM), that have not been observed yet. The last category consists of an artefact due to the modification of the Newtonian gravitational law called Modified Newtonian Dynamic (MoND) [19]. This last hypothesis, challenged by the observation of the Bullet cluster, will not interest us in this analysis and will therefore not be elaborated here.

2.2.1 Baryonic Dark Matter

Some of the dark matter postulated above must be baryonic. Indeed, the amount of baryonic matter deduced from the nucleosynthesis of the Big Bang $\Omega_{bar} \approx 0.04$ is higher than what is observed from the luminous matter $\Omega_{lum} \approx 0.01$ [22]. Some of this non-luminous matter might be found in the form of Massive Astronomical Compact Halo Objects (MACHOs), *e.g.* planets, brown dwarfs or primordial black holes. Furthermore, studies of galaxies clusters have revealed the presence of gas in vast amount in those clusters. Nevertheless, the baryonic matter alone can not explain the behaviour of the rotation curve of spiral galaxies 2.1. In fact, the contribution of the

baryonic matter to the total estimated density of dark matter is believed to be under 15% **[BaryonicMatter]**.

2.2.2 Non-Baryonic Dark Matter

The observational evidences constrain the properties of new particles postulated to be dark matter. First, these particles must not interact via strong force, *i.e.* they must be colour neutral. Similarly, these new particles must be electrically neutral since dark matter is expected to have no electro-magnetic interaction. Interaction via weak nuclear force are still permitted, but the interaction cross-section of dark matter with ordinary matter must be smaller than the one between baryonic matter since it has not been observed yet. Finally, the dark matter must be stable for at least the life time of the Universe, τ_U, in order to explain the recent observations.

Non-baryonic dark matter candidates are particles that are not predicted by the standard model. Three categories can be distinguished following their speed : hot, warm and cold dark matter. Candidate particles with masses of 1 keV or below are forming the so-called hot dark matter, e.g. neutrinos and axions. The warm dark matter consist of particles with masses ranging from 1 keV to 10 GeV/c^2, of which sterile neutrinos could be an example. The cold dark matter, consisting of particles with mass above a few MeV, is the more commonly accepted category. Dark matter has also a role in the evolution of the Universe and the formation of the galaxies. In fact, dark matter particles must be cold, *i.e.* non-relativistic, in order allow the galaxies formation in the current state of the Universe. Indeed, the formation and evolution of galaxies can be simulated using a N-body simulation, in which a cold dark matter scenario is preferred to a hot or warm dark matter scenario.

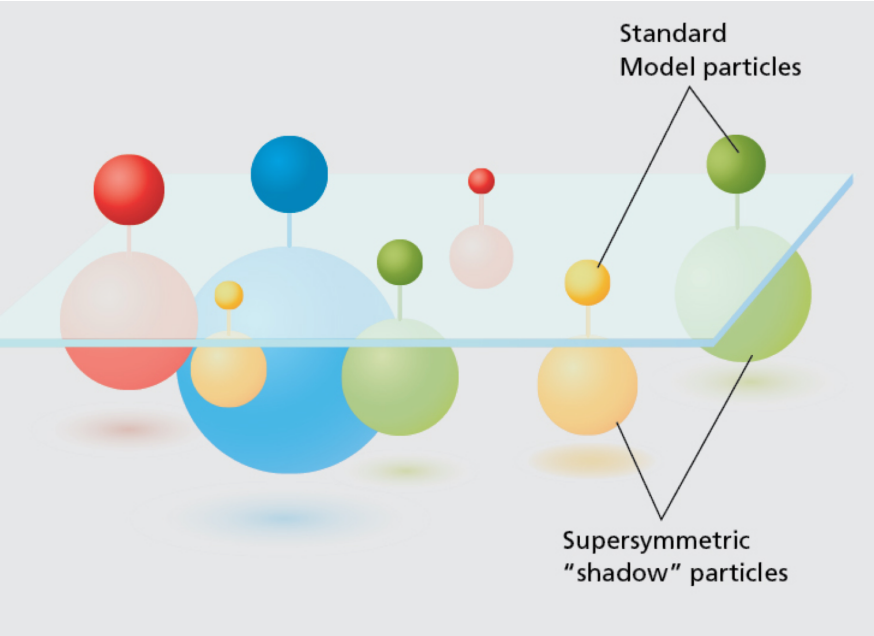

FIGURE 2.3: Schematic representation of supersymmetric particles in regards to their standard model equivalent.

Currently, the most popular candidates for dark matter particles are Weakly Interacting Massive Particles (WIMPs). These WIMPs are expecting to have been produced

thermally in the early Universe, along with SM particles. In order to obtain the dark matter abundance we are observing today, the self-annihilation cross-section required is $\langle \sigma \nu \rangle \sim 3 \times 10^{-26}$ cm^3 s^{-1}. This cross-section corresponds approximately to what is expected for a new particle with a mass of roughly 100 GeV interacting via weak force. Such particle happens to be predicted by the super-symmetric (SUSY) extension of the SM, leading to the "WIMP miracle".

Thus, SUSY particles are suitable candidates for WIMPs. These particles consist of a super symmetric extension of the standard model. Which means that each fermion in the SM has a bosonic super-partner of spin 1/2 in the SUSY model, as well as each boson will have a fermionic super-partner of spin 0. This analysis will assume dark matter to be composed of WIMPs, which will be denoted by χ. The lightest SUSY particles (LSP) is the neutralino, a neutral fermion.

2.3 Dark Matter Detection

Three main detection principles can be used while searching for evidence of dark matter which are direct detection, indirect detection, production. These three methods can be represented with different orientation of the Feynman diagram describing the interaction of WIMPs with standard model (SM) particles (see fig. 2.4). Direct detection experiments search for scattering of SM particles with dark matter particles (WIMPs). Indirect detection experiments try to detect the primary and secondary particles created in WIMPs pair-annihilations, *e.g.* neutrinos, photons, antiparticles. Particles accelerators attempt to find evidences of dark matter by its production in collisions of SM particle such as the proton-proton collision of the Large Hadron Collider (LHC) at CERN.

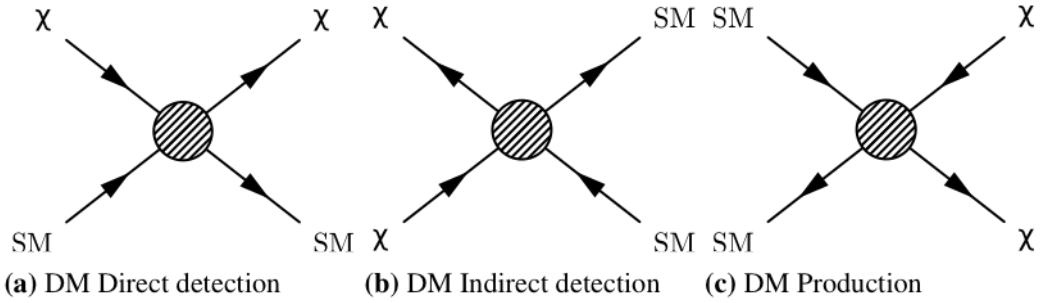

FIGURE 2.4: Simplified Feynman diagrams for WIMPs interaction with standard model particles (SM) with different time ordering. (a) WIMPs-SM particles scattering (direct detection), (b) WIMPs annihilation (indirect detection), (c) WIMPs pair-production from SM particles [6].

2.3.1 Direct Search

The aim of direct detection experiments is to measure the elastic scattering cross-section of WIMP with ordinary matter $\sigma_{\chi-N}$, through the detection of WIMPs scattered by target nuclei. By measuring the recoil of the nucleus, the recoil energy Q can be measured either via its heat deposition in the medium (using phonons), the production of scintillation radiation from excited target atoms (using photons), or the ionization of the medium (using electrons). Indirect detectors commonly use the measured energy-ratio

between two such technologies to discriminate background from signal events. Since the signal is expected to be very small due to the weak cross-section of such interaction, direct detection experiments aim to operate at extremely low background. Liquid noble gas detectors, such as XENON [30], LUX [17] and Dark-Side [1], look for scintillation and ionization signals. Whereas cryogenic detectors, e.g. CDMS [39], CoGeNT [25], EDELWEISS [27] and CRESST [28], use semi-conducting or scintillating crystals to measure phonons from the heat deposition in combination with ionization or scintillation.

Another approach is to look for annual modulations of the WIMP-nucleon recoil rate in a crystal. These variations may arise from the movement of the Earth around the Sun, during which different DM velocity distributions are encountered. The DAMA-LIBRA [4] experiments, using this technique with sodium iodine (NaI) crystal, claimed to have observed such an annual variation. They reported a measured modulation with a 8σ significance and consistent with detection of WIMPs with $\sim$ 60 GeV/c^2 mass in the galactic halo [5]. The DAMA results remain highly controversial since other experiments like CDMS, XENON or EDELWEISS have explored the same parameter space without being able to confirm this claim.

2.3.2 Particle Accelerator Production

Dark matter could also be produced in particle collisions at particle accelerators, such as the TeVatron [**TeVatron**] and the Large Hadron Collider (LHC) [**LHC**]. However, the produced dark matter will escape the detector without being seen due to their weak interaction cross-section. Thus, these experiments are looking for missing transverse energy signals (ME_T), which is potentially linked to dark matter. Usually, the technique encountered in dark matter production searches consists of looking for SUSY particles. Since they are heavy and unstable, SUSY particles might decay to dark matter candidate particles. This analysis are thus looking for missing E_T and specific SM particles predicted final states.

2.3.3 Indirect Search

Indirect detection experiments search for standard model particles created in dark matter self-annihilations, such as photons, neutrinos. These experiments usually focus on regions with in which a high density of dark matter is expected like the centre of heavy celestial bodies, e.g. the Sun, and Earth. A dense WIMP population is also expected in the Galaxy Centre. Various type of experiments are looking for an excess of signal coming from these directions in a defined energy range. Ground γ-ray experiments such as H.E.S.S. [29], MAGIC [**MAGIC**] and VERITAS [31] as well as the Fermi satellite are looking for γ-rays produced by WIMP annihilations. Due to size restriction, satellite experiments are usually focusing on the detection of photons in the keV to GeV energy range. While, without this size restriction, ground based detectors are able to detect higher energies up to TeV energy scale. Neutrino telescopes, such as IceCube, ANTARES and Super-Kamiokande [33], are looking for high-energy neutrinos coming from these locations. Other experiments, e.g. PAMELA [37], Fermi [32] and the AMS-2 [36], are looking for an anti-matter flux from dark matter annihilations. These latter three experiments reported an increased positron flux at high energies above expected background which could be explained by a signal from WIMP annihilations in the TeV energy range. However, this excess is also consistent with pulsars and supernovae

remnants, which provide a more standard astrophysical explanation. In this work, we will focus on neutrino signal from the Galactic Centre.

2.4 Dark Matter Distribution in Galaxies

Even if we still have no certitude of what composes the dark matter, the understanding of its distribution in the Universe keeps on improving. The distribution of dark matter in the Universe can be modelled using the measurements of stars radial velocities and weak gravitational lensing along with numerical N-body simulations [**NBodysimu**]. Different profile functions can be used to describe the distribution of dark matter in galaxies, like the Navarro-Frenck-White (NFW) profile [14] and the Burkert profile [**Burket**]. These profiles can be formulated as in the following general profile function :

$$\rho_\chi(r) = \frac{\rho_0}{(\delta + \frac{r}{r_s})^\gamma . (1 + (\frac{r}{r_s})^\alpha)^{\frac{(\beta-\gamma)}{\alpha}}} , \tag{2.3}$$

where ρ_0 and the scale radius r_s are parameters which will vary with the halo model. The value ρ_r is the dark matter density at the scale radius. The parameters α, β, γ and δ are dimensionless parameters that depend on the halo model used. The values of these parameters for the NFW profile and the Burkert profile can be found in table 2.1. The parameter δ was introduced in order to represent an even broader set of dark matter profile than the Zhao profile [**Zhao**]. This equation include "cusped" profile, which diverge for $r \to 0$, as well as bulked profile, which does not have a divergent cusp at $r = 0$. The "cusped" profile, like the NFW halo profile, give a very concentrated signal, which will appear almost point-like for halos located at large distances. While "bulked" profile, as the Burkert profile, will appear wider making signal from these halos more difficult to detect in indirect searches. In both cases, the the density profile of the DM approaches zero at large distances in order to have a finite mass for the galaxies. In this analysis, we will use the NFW density profile with the parameters taken from [8] and expressed as :

$$\rho_\chi(r) = \frac{\rho_0}{\frac{r}{r_s}(1 + \frac{r}{r_s})^2} . \tag{2.4}$$

where the parameters used can be found in table 2.1.

Parameter	Units	NFW profile	Burket profile
$(\alpha, \beta, \gamma, \delta)$	-	(1,3,1,0)	(2,3,1,1)
ρ_0	$10^7 M_\odot/\text{kpc}^3$	$1.40^{+2.90}_{-0.93}$	$4.13^{+6.2}_{-1.6}$
r_s	kpc	$16.1^{+17.0}_{-7.8}$	$9.26^{+5.6}_{-4.2}$

TABLE 2.1: Dark matter halo profile parameters for the NFW profile and the Burket profile as taken from [8]

2.5 Dark Matter Signal Intensity From the Galactic Centre

As already explained, dark matter might be subject to self-annihilation into standard model particles. The intensity of WIMP annihilation is proportional to the square of the dark matter density distribution in the galactic halo since two particles are needed for an annihilation. The spatial distribution of the signal particles is described by the J-Factor. The J-Factor is defined as the integral of the squared dark matter density along the line-of-sight, l, **[J_factor]**

$$J_a(\Psi) = \int_0^{l_{max}} \rho_\chi^2 \left(\sqrt{R_{sc}^2 - 2\, l\, R_{sc}\, \cos(\Psi) + l^2} \right) \mathrm{d}l \ , \tag{2.5}$$

where Ψ denotes the opening angle to the galactic centre, R_{sc} is the radius of the solar circle ($R_{sc} \simeq 8.5$ kpc) and ρ_χ is the dark matter density profile as define in equation 2.4. The shape of the J-factor strongly depends on the halo model used. The quantity l is the distance along the line of sight and the upper integration limit l_{max} is a quantity which depends on the radius of the galactic halo R_{halo} and can be expressed as

$$l_{max} = \sqrt{R_{halo}^2 - \sin^2 \Psi\, R_{sc}^2} + R_{sc}\, \cos \Psi \ , \tag{2.6}$$

where the radius of the galactic halo is chosen to be the radius of the Milky Way $R_{halo} = 50$ kpc. Due to the rapid decreases of the density function for radii above the scale radius r_s, these radii do not have a significant contribution to the total value of the J-factor. This behaviour can be seen in fig. **??** showing the J-factor as function of the opening angle to the Galactic Centre.

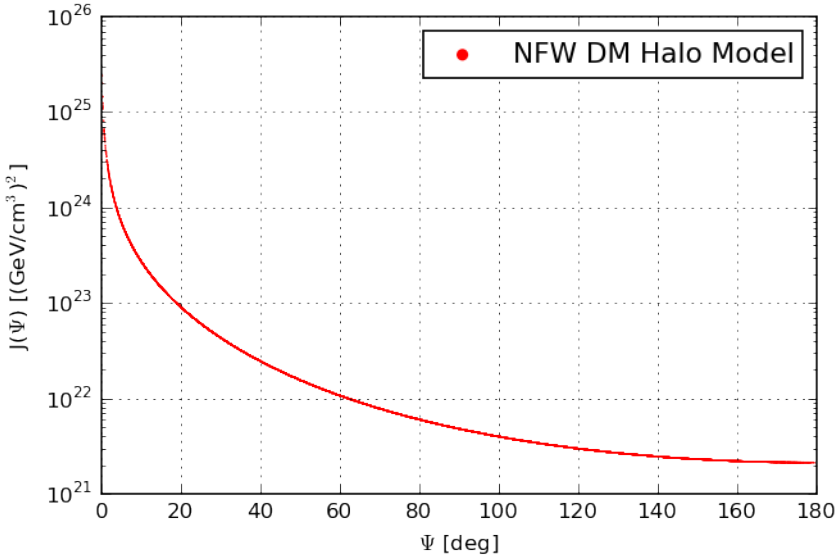

FIGURE 2.5: J-factor calculated for the NFW halo model as a function of the opening angle Ψ for the IceCube IC86 Low Energy Galactic Centre analysis.

The J-factor is also needed to calculate the energy-differential flux of neutrinos resulting from DM annihilation [**diff_flux**]

$$\frac{\mathrm{d}\phi_\nu(\Psi)}{\mathrm{d}A\,\mathrm{d}\Omega\,\mathrm{d}t\,\mathrm{d}E} = \frac{\langle\sigma_A\nu\rangle}{2}\,\frac{J_a(\Psi)}{4\pi\,m_\chi^2}\,\frac{\mathrm{d}N_\nu}{\mathrm{d}E}\,, \tag{2.7}$$

which also depends on the WIMPs thermally averaged product of the self-annihilation cross-section, $\langle\sigma_A\nu\rangle$, the inverse of the squared WIMP mass, m_χ, and the neutrino energy spectrum per annihilating WIMP pair, $\mathrm{d}N_\nu/\mathrm{d}E$ [**netrinoFlux**]. The fact that there are two WIMPs per annihilation is accounted by the factor $1/2$. We consider WIMPs to be Majorana particles, i.e. WIMPs are their own anti-particles. The factor $1/4\pi$ accounts for the isotropic emission of neutrinos.

The annihilation of two WIMPs will in first instance lead to a pair of SM particles, one particle and its associated antiparticle. The model used in order to describe dark matter influences the branching ratio for each type of particle. In this analysis, five different annihilation channels have been considered assuming a 100% branching ratio (B.R.) :

$$\chi\chi \to b\bar{b},\ W^+W^-,\ \nu_\mu\bar{\nu_\mu},\ \mu\bar{\mu},\ \tau\bar{\tau}. \tag{2.8}$$

After the first annihilation, the Standard Model particles created will, in most case, decay into lighter particles, including neutrinos. In the case of a leptonic primary particles, the decay will automatically creates a neutrino due to the leptonic flavour conservation. And as a matter of fact, weak gauge bosons could produce charged leptons and neutrinos while decaying.

$$W^\pm \to l^\pm\,\nu \qquad (B.R. \sim 30\%) \tag{2.9}$$
$$W^\pm \to q\bar{q} \qquad (B.R. \sim 70\%) \tag{2.10}$$

In addition, gluons and quarks will be the source of hadronic showers which produce mostly neutrinos via the decay of mesons produced in the shower. The $b\bar{b}$ channel is expected to produce fewer neutrinos than other annihilation channels since, in the case of quarks, neutrinos will mostly be produced in hadronic showers rather than directly. The $b\bar{b}$ channel will thus have the softer neutrino spectra, while the channel $\nu_\mu\bar{\nu_\mu}$ will have the hardest spectra.

The average neutrino spectra per annihilation process ($\mathrm{d}N/\mathrm{d}E$) for these masses and for each annihilation channel were computed using PYTHIA simulation package [**Pythia**] and are shown in Fig.2.6.

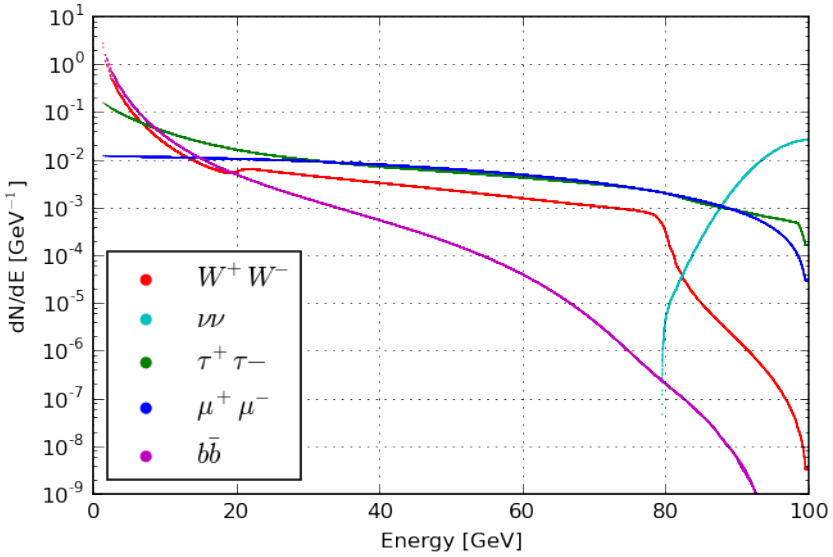

FIGURE 2.6: Neutrino energy spectrum for the annihilation of WIMP of 100 GeV/c^2 mass to ν_μ final product through $b\bar{b}$, W^+W^-, $\nu_\mu\bar{\nu}_\mu$, $\mu\bar{\mu}$, and $\tau\bar{\tau}$ annihilation channels.

Finally, the neutrinos produced in the decay of the annihilation products need to reach the detectors travelling from the place of the WIMPs annihilation. Thus, the neutrino energy spectra are influenced by the neutrino absorption that could occur in the source medium, such as in the Sun. On their way to Earth, neutrinos will also be subject to the neutrino oscillation, leading to a 1:1:1 ratio of neutrino flavours at the detector location when sources much larger than the oscillation length are considered.

Chapter 3

Neutrinos Astronomy

Neutrinos are electrically neutral particles interacting weakly with matter. Having these properties, neutrinos seem to be an ideal astrophysical messengers. Since they interact weakly with matter, neutrinos are not absorbed by dense regions and are thus able to carry information about regions opaque to photons. Furthermore, neutrinos are neutral particles, which means they are not deflected by magnetic field on their way to Earth. which makes it easier to pinpoint the direction of the neutrino source. High energy neutrinos are expected to be produced by some of the most cataclysmic and interesting events in the Universe, *e.g.* exploding stars, gamma ray bursts, supernova remnants, neutrons stars or annihilation of dark matter.

3.1 Neutrinos Interaction with matter

Neutrinos are elementary particles belonging to the lepton family (fermions with $1/2$ spin). There are three flavours of neutrinos, electron neutrinos (ν_e), muon neutrinos (ν_μ), tau neutrinos (ν_τ), as well as their corresponding anti-particles. Neutrinos interact with matter only by weak nuclear interaction through the exchange of Z^0 bosons (neutral current) or $W^\pm$ bosons (charged current). As a result, neutrinos have very low interaction cross-sections, yet increasing linearly with energy [**Sylvie**]. Since neutrinos are neutral particles, their existence is deduced from the charged lepton production during their charged current interaction following these equations

$$\nu_l + N \rightarrow l^- + X \ , \tag{3.1}$$
$$\bar{\nu_l} + N \rightarrow l^+ + X \ , \tag{3.2}$$

where N denotes a nucleon, X is the final hadronic product and l stand for the three different flavours of neutrinos ($e^\pm$, $\mu^\pm$, $\tau^\pm$). In the charged current interaction, neutrinos turn into their associated charged leptons in order to preserve the lepton number. The neutral current interaction can be seen as a scattering of the initial neutrino by the nucleus, N, with a hadron or a hadronic shower, X, in the final state

$$\nu_l + N \rightarrow \nu_l + X \ , \tag{3.3}$$
$$\bar{\nu_l} + N \rightarrow \bar{\nu_l} + X \ , \tag{3.4}$$

Depending on the energy of the neutrinos, three main types of scattering process with the nucleon may occur [10]. The first one is the Quasi-Elastic Scattering (QES) in which the target nucleon remains almost unchanged and the quasi-totality of the incident momentum is transferred to the out-going lepton. For neutrinos with energies

around 1 GeV to 10 GeV, the Nuclear Resonance Production (NRP) interaction dominates. In that specific case, neutrinos can excite the target nucleon to a resonance state. **The baryon resonance thus created conducts to a hadronic system**. Neutrinos with an energy above 10 GeV are able to interact with the quarks in the nucleon and diffuse them individually. This process, called *Deep Inelastic Scattering*, dominates at energies greater than **10 GeV**. The neutrino breaks the original nucleons and create an hadron shower as shown in the fig. 3.1. Four specific cases can be distinguished, taking into account the neutrino flavour and the type of interaction (neutral or charged current). For both neutral current and charged current interaction, a hadronic shower is produced.

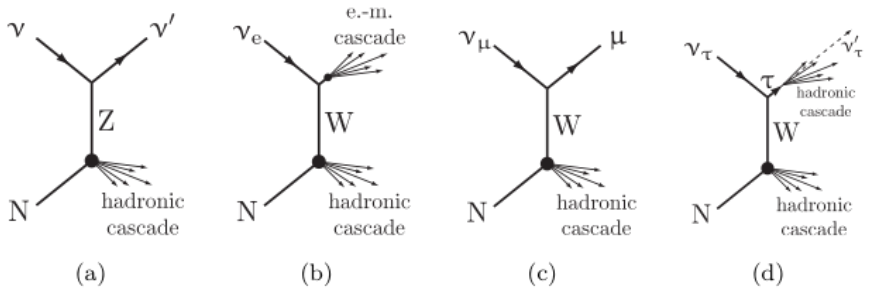

FIGURE 3.1: Diagrams showing the high-energy neutrinos interactions in the the detector dielectric medium : (a) Neutral current interactions, (b)-(d) Charged current interactions for ν_e, ν_μ, ν_τ respectively. Taken from [15].

For charged current interactions, we can differentiate three specific cases depending on the neutrino flavour. This distinction arises from the behaviour of their associated leptons in the detector medium. Therefore, the signature in the detector will be typical for each neutrino flavour (cf. figure 3.2).

Electron neutrinos While interacting with the medium, electron neutrinos create electrons or positrons, e^- or e^+. These electrons lose their energy in electromagnetic showers and are not able to travel more than a few meters in the detector medium (ice or water). Thus, the electron neutrino interaction create a "cascade signature" in the detector. These events give us a poor angular resolution as a result of their "cascade-like" shape.

Muon neutrinos The muon, μ^+ or μ^-, resulting of the muon neutrino charged current interaction propagates in straight line and is almost aligned with the original neutrino (especially true at high energy). These features provide angular resolutions as good as $< 1°$, which is valuable for the quality of the event reconstructions. The events caused by a muon neutrino are called "track-like" events.

Tau neutrinos Tau leptons, τ^+ or τ^-, have a short lifetime (2.8×10^{-13} s) which does not allow them to travel far in the detector medium. While decaying, $\tau^\pm$ are generally at the origin of a second particle shower. Tau leptons have 83% probability to decay in an electron or hadron, thus creating an electromagnetic or hadron shower. This event topology is known as "Double Bang". There is also 17% probability for the tau to decay in a muon, producing a track [**PDGtau**].

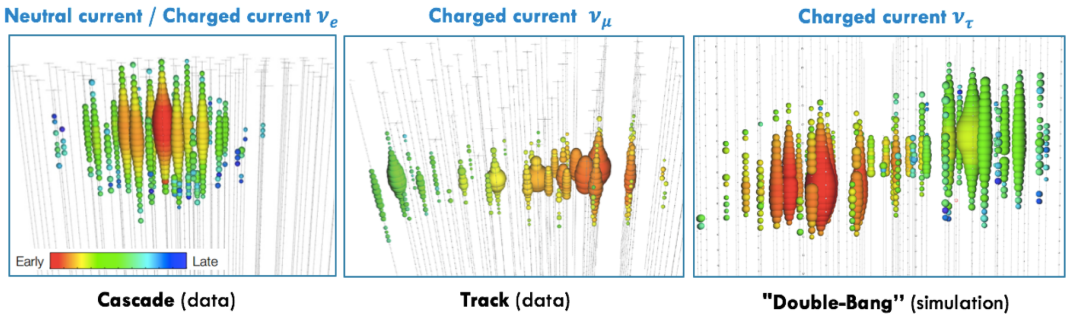

FIGURE 3.2: Signature of events in the detector. Neutral current and charged current interaction of ν_e are responsible for a cascade-like signature in the detectors. Events having for origin the charged current interaction of ν_μ will be seen as track-like events in the detectors. Finally, the charged current interaction of a ν_τ in the detectors volume will have a "double bang" signature.

3.2 Expected Sources of Neutrinos

The energy of the detected neutrinos gives us information about how and where it could have been produced. Following this idea, we can divide neutrinos in two main categories : low-energy and high-energy neutrinos. Low-energy neutrinos have energies up to few tens of MeV, while the high-energy category is composed of neutrinos with energies above 10 GeV. This division, while arbitrary, reflects the production process of these neutrinos. Moreover, these two categories of neutrinos will require different ways of designing the detectors. For instance, Cherenkov detector under water or in ice, like ANTARES and IceCube, are designed to operate in the region from tens of GeV to about 100 PeV. On the other hand, underground detectors, *e.g.* Super Kamiokande [**superkamiokande**] or Borexino [**borexino**], operate in the energy range from keV to several GeV.

3.2.1 Low-Energy Neutrinos

The lowest energy neutrinos are called cosmological neutrinos or Cosmic Neutrino Background (CNB ou CνB), with energy ranging from μeV to few meV (cf. figure 3.3). Similarly to the cosmic microwave background (CMB), the CνB is a relic of the Big Bang, with information carriers being neutrinos instead of photons [**CNB1**]. The CνB give us a glimpse of the Universe one seconde after the Big Bang, while the CMB decoupled when the Universe was 379,000 years old [**CMB**]. The neutrinos from the CνB are the oldest relics of the Big Bang. From the temperature of the CMB, $T_\gamma = 2.725 \pm 0.001$ K [3], the temperature of the CνB can be estimated to be $T_\nu \approx 1.95$ K . These neutrinos, however, are not detectable with the current technology as their interaction cross-section is very low.

Another contribution to the low-energy neutrinos are those produced in nuclear reactions such as the ones occuring in the Sun or in the heart of Supernovae. These neutrinos have energies from few eV up to few GeV. These low energy neutrinos are not detectable by telescope such as IceCube or ANTARES. Howerver, underground neutrino detectors aims to detect solar neutrinos as well as geoneutrinos and neutrinos from artificial nuclear sources [**LowEnergyNeutrinos**].

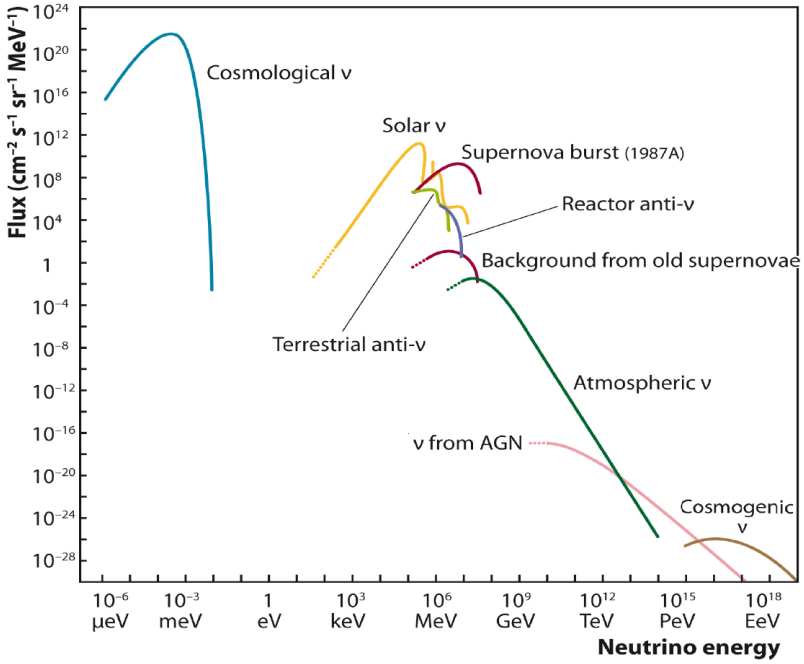

FIGURE 3.3: Measure and expected fluxes of natural and reactor neutrinos. [].

3.2.2 High-Energy Neutrinos

The so-called high-energy neutrinos are mainly produced in high-energy particle collisions, which produce mesons soon decaying to neutrinos as well as other particles. The produced neutrinos will travel through space in straight line and if detected on Earth, will point right back to their sources.

Atmospheric Neutrinos : The Earth is constantly hit by cosmic rays, which are charged particles whose energy can reach very high values (10^{15} to 10^{20} eV). These cosmic rays, are one of the sources of high-energy neutrinos. When cosmic rays enter the upper atmosphere, the primary incident CR particles produce unstable particles with short lifetime. The secondary particles created in these interaction are highly energetic and ultra-relativistic. These secondary particles will either interact with atmospheric molecules or decay to lighter particles, as muons and neutrinos.

$$p^+ + N \rightarrow \pi^{\pm} + X \tag{3.5}$$
$$\pi^+(\pi^-) \rightarrow \mu^+(\mu^-) + \nu_\mu(\bar{\nu}_\mu) \quad (\sim 100\,\%\, b.r.) \tag{3.6}$$
$$\mu^+(\mu^-) \rightarrow e^+(e^-) + \nu_e(\bar{\nu}_e) + \bar{\nu}_\mu(\nu_\mu) \quad (\sim 100\,\%\, b.r.) \tag{3.7}$$

where N is the initial atmospheric nucleon and X is its hadronic remains. The muons created spread among the Earth surface and are capable of travelling a few tens of kilometres into the Earth before interacting. On the other hand, atmospheric neutrinos are capable of crossing the Earth without interacting with a nucleus. Atmospheric muon and neutrinos are the main background source of neutrino telescope such as IceCube or ANTARES.

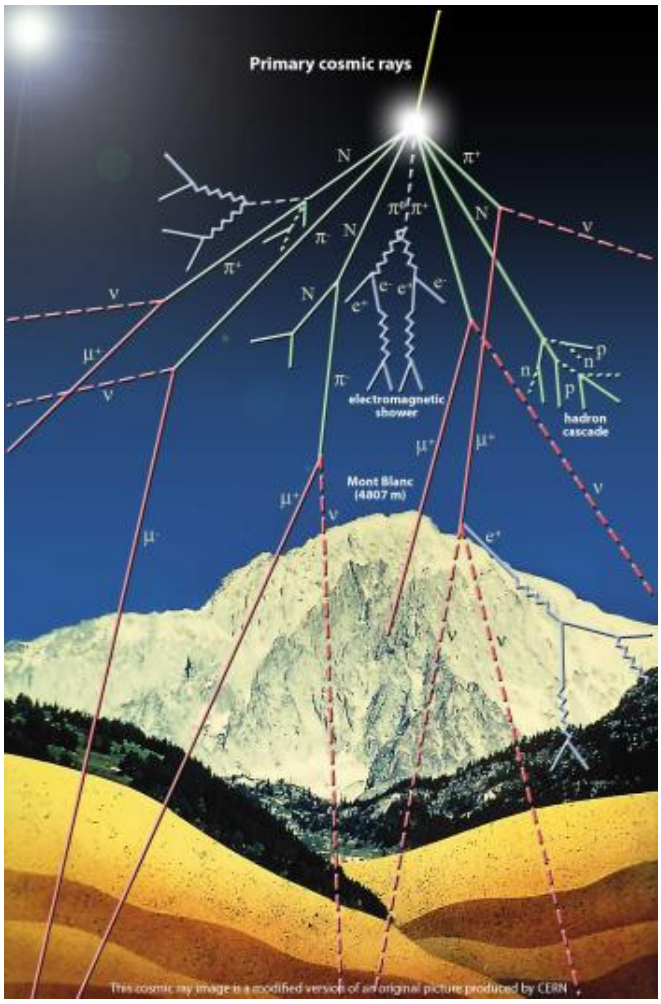

FIGURE 3.4: Schematic view of Cosmic Ray interaction in the upper atmosphere.

Astrophysical neutrinos : There are several candidates to explain the origins of high-energy cosmic rays. Yet, the sources of these cosmic rays are believed to produce high-energy neutrinos as well. One of the sources could be in the form of Active Galactic Nuclei (AGN), *e.g.* galaxies with a super massive black hole in their centre. When matter in the galaxy fall in the black hole, a jet structure is created emitting large amounts of energy. These jets could accelerate protons to high energies. Neutrinos are also believed to be produced in these gamma ray sources. Another potential source are Gamma Ray Burst (GRB) which are the most energetic events observed in the Universe. GRBs consist of short pulses of gamma ray lasting from a fraction of a second up to 100 seconds. These events are located really far away from Earth and their origin is still unknown. Possible explanations are that these events origin from colliding neutron stars or massive stars collapsing into a black hole. These collisions will produce mainly π mesons rapidly decaying to muons and neutrinos. These muons (μ^+) will, in turn, decay and give an electron (e^+) and two neutrinos (ν_e and $\bar{\nu}_\mu$), as shown in equation 3.2.2. r volume. IceCube is the first cubic-kilometre neutrino detector. In 2012, IceCube announced the detection of two neutrinos with energy around 1 PeV, known as Bert and Ernie. These neutrinos events are the most energetic ever observed. Such high-energy neutrinos can only be detected by a detector of very large detector.

Cosmogenic neutrinos : Cosmogenic neutrinos are produced in the interaction of ultra high energetic cosmic rays (UHECRs) with the photons of the CMB. These neutrinos are also called GZK neutrinos as the phenomenon responsible for their creation is also the source of a strong feature in the CR energy spectrum known as the GZK cut-off. Cosmogenic phenomenon are expected to be the main source of neutrinos with energies from 100 PeV to 10 EeV. The expected flux of cosmogenic neutrinos is very low, requiring an important detector volume and a long exposure in order to be detected. However, the detector volume is still unknown.

Neutrinos from Dark Matter : Neutrinos with high energies could also come from the annihilation of dark matter. As explained in chapter 2, there is evidence of "unseen matter" in the Universe, the so-called dark matter. One of the favourite candidates for this new type of matter are Weakly Interacting Massive Particles (WIMPs) that were created during the Big Bang simultaneously with ordinary matter. Dark matter particles would scatter in massive objects such as the Sun or the Earth, lose energy and become gravitationally trapped, accumulating in the centre of the object. These dark matter particles would annihilate and create, among others, neutrinos with energies above the one coming from nuclear reactions. The observation of these high-energy neutrinos coming from the Sun or the Earth would be a very clean signal of dark matter. Other stellar objects are expected to contain dark matter, such as the centre of galaxies. This analysis will focus on the search of WIMPs from the centre of the Milky Way.

Chapter 4

Neutrino Telescope

Given the low interaction cross-section of neutrinos, their observation requires a large volume of target material. The two detectors used in this analysis, ANTARES and IceCube, managed to obtain such a large detector volume by placing a sparse array of photodetectors in deep, dark, and dielectric environments, respectively sea water and the Antarctic ice. Both telescopes are Cherenkov detectors optimised for the search of high-energy neutrinos, such as the neutrinos coming from dark matter annihilation. The working principle of these neutrino observatories, as well as a comparison of their geometry and performance, will be presented in this chapter.

4.1 Detection Principle

As mentioned earlier, neutrinos are not detected directly but indirectly from their interaction with a nucleus in the detector volume. When occuring at high energy, such interactions are creating relativistic and electrically charged secondary particles. This charged particles will emit Cherenkov radiations while going faster than the speed of light in the dielectric medium of the detector [2]. This phenomenon is the result of the coherent superposition of electromagnetic waves due to the polarisation of the medium by the passing particle.

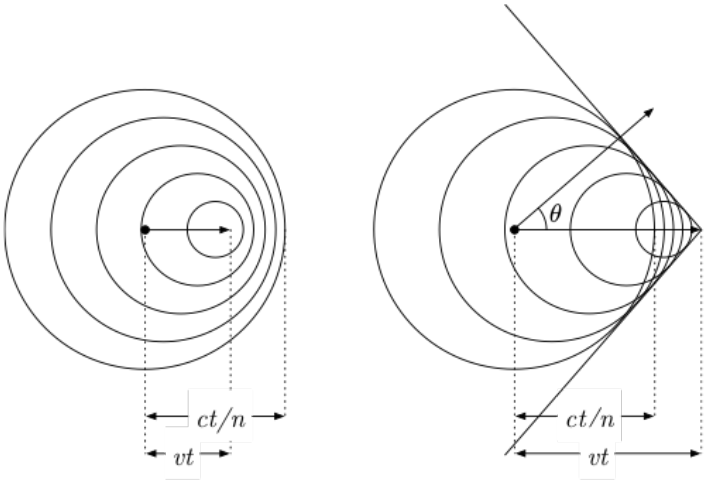

FIGURE 4.1: **Left :** Case of a particle moving with $v < c/n$. **Right :** Emission of Cherenkov radiations for particles with a speed $n > c/n$ [20].

If the speed of the particle is greater than the c/n ratio (where n is the refractive index of the medium and c is the speed of light), there is formation of a light cone with

an half aperture angle θ_c, see figure 4.1. So, the Cherenkov light is emitted with a characteristic angle depending of the particle speed and given by the following equation

$$cos\theta_c = \frac{1}{n\beta} \ , \tag{4.1}$$

where $\beta = v/c$, v being the speed of the particle in the medium. Assuming a relativistic particle ($\beta \sim 1$) in a medium with a refractive index of $n = 1.333$ for water **[PDF_anglewater]** and $n = 1.309$ for ice **[PDG_angleice]**, the value of these characteristic angles are respectively $\theta_c \sim 41°$ and $\theta_c \sim 40°$. The number of Cherenkov photons produced by a particle of charge e, per unit of length, x, and unit of wavelength, λ, is given by the Frank-Tamm formula [34] :

$$\frac{d^2N}{dxd\lambda} = \frac{2\pi\alpha}{\lambda^2}\left(1 - \frac{1}{n^2\beta^2}\right) \ , \tag{4.2}$$

with α being the fine-structure constant with the value $1/137$. Since the number of photons produced is inversely proportional to the wavelength, the contribution of smaller wavelenght is more significant. For this reason, the spectrum peaks in the UV region, causing the produced light to appear blue to the naked eye. In ice, a relativistic particle produce about 330 photons per centimetre of track in the wavelength interval from 300 to 600 nm. This wavelength interval happen to match the typical sensitivity region of the IceCube optical sensors [12]. For the ANTARES detector, almost 200 optical photons per centimeter are expected in the sensitive region of the photomultiplier tubes, *i.e.* 350 nm $\leq \lambda \leq$ 600 nm [16].

4.2 IceCube

IceCube is a cubic-kilometer neutrino observatory located at the South Pole. The main goal of this experiment is the detection of neutrinos from astrophysical sources. IceCube is burried in the Antartic ice at a depth of 2450 meters. The observatory is completed with a surface cosmic ray detector (IceTop), as well as a denser instrumented inner sub-detector (DeepCore) to lower the energy threshold.

4.2.1 Detector Configuration

The IceCube observatory consists of 5,160 photomultupliers tubes (PMTs) (DOMs) attached to vertical strings placed into 86 boreholes. Seventy-eight of these strings are deployed on an hexagonal grid with a spacing of 125 meters between each borehole which holds 60 PMTs, disposed from 1,450 to 2,450 metres depth with a vertical separation of 17 meters, see figure 4.2. The detector design is optimised for the search of high-energy astrophysical neutrinos above $\sim$ 100 GeV. The IceCube detector includes a dust layer, which corresponds to a layer of volcanic ashes located at a depth of 1970 to 2100 meters below the surface.

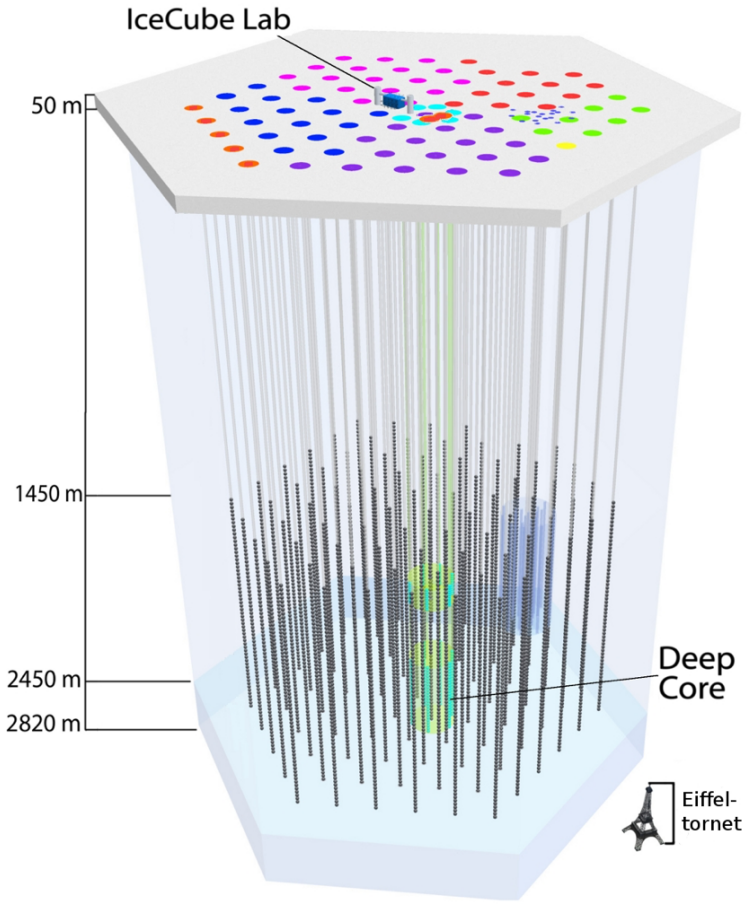

FIGURE 4.2: IceCube detector configuration [**website:IceCube**].

The PMTs in IceCube are housed in Digital Optical Modules (DOMs). These DOMs are the basic detection units of IceCube. Each DOM is composed of a 25 centimetres diameter downward oriented PMT, along with a DOM mainboard (DOM MB) to process and digitalise the signal. The PMT and DOM MB are housed in a 13 mm thick pressure-resistant glass sphere. There is a cut-off on the wavelenght detectable by the DOMs, this limit being around 350 nm.

The detection of optical photons is done in the following way : first the photon reaches the DOM and crosses the glass sphere to reach the PMT. The photon is then absorbed by the photo-cathode of the PMT and a photo-electron (pe) is emitted and amplified to a factor of 10^7 when passing through the dynodes. Further processing is triggered when there is a hit, i.e. when the anode voltage exceeds 0.5 pe, with 1 pe corresponding the anode voltage for one single photo-electron being amplified through all dynodes. These hits are labelled as Hard Local Coincidence (HLC) if at least two neighbouring DOMs record a hit within a time window of 1 μs.

Once triggered by photons, the DOMs digitized the trigger hit and send the digitize signals to the surface computers. Once received on the surface, algorithms check for correlation of these hits within a defined time window in order to reduce the noise rate. The information of triggered events are then regrouped into events that are reconstructed and filtered (cf. section 4.2.2) in order to reduce the raw data stream even further. This first data reduction is referred to as Level 1. This reduced data stream is then sent to the data warehouse at the University of Wisconsin (UW) Madison via

satellite, where it can be accessed by the entire collaboration for further processing and analysis. This processing state, where more sophisticated reconstructions are calculated for each events, is often referred to as Level 2.

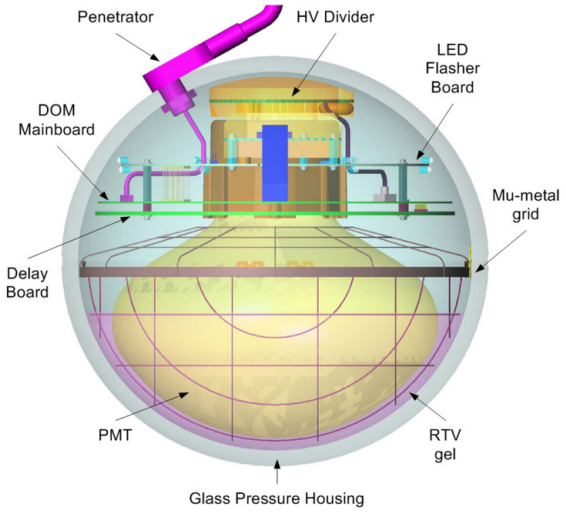

FIGURE 4.3: Schematic drawing of a Digital Optical Module (DOM) used in IceCube [].

DeepCore : The eight remaining strings are deployed more compactly in the centre of the array, forming the DeepCore subdetector. A horizontal spacing of 70 metres can be found between each string and each DOM is separated by a 7 metres vertical space. The first ten DOMs of each string are located above the dust layer while the remaining DOMs are beneath it. This configuration makes it possible to detect neutrinos above ~ 100 GeV, enabling the study of neutrino oscillation. Since low-energy muons ($E_\mu = 10$ GeV) travel about 5 meters per GeV in the ice, the spacing of the standard DOMs of IceCube leads to a minimum energy threshold for neutrinos of 50-100 GeV [38]. The higher module density, thus enable a lowering of this detection threshold. In order to improve the capabilities of DeepCore, the sub-detector uses the standard DOMs of IceCube as a veto to background.

IceTop : IceTop is composed of 81 surface stations, each consisting of two tanks each equipped with two downward facing DOMs. IceTop detects air-shower from primary cosmic rays in the 300 TeV to 1 EeV range. The IceTop stations are located on top of IceCube strings. Even if its primary goal is the detection of cosmic rays, IceTop also act as a veto for cosmic muons and a calibration detector for IceCube.

4.2.2 Event Filtering, Cuts and Veto

The majority of the events triggering IceCube optical digital modules are atmospheric muons, which are part of the background. In order to reduce the rate of these events, on-line as well as off-line filters have been developed. Events are tags depending on either they fulfils or not different conditions, such as restrictions on the energy, the direction or the topology of the event. Each filter has its own purpose and we will only present here the ones that were used for our analysis. A brief description of the filters, cuts and vetoes used in this analysis will be found in this section.

DeepCore Filter : The purpose of the DeepCore filter is to select events starting inside the DeepCore fiducial volume, rejecting at the same time atmospheric muons. This filter algorithm applies a simple veto to the cosmic ray muon background events, dominating the low-energy data set. First, a selection of the hard local coincident hits within the DeepCore subdetector is performed. The centre of gravity (COG) of these selected hits is then computed. This information is used by an algorithm looping over all the HLC in the IceCube detector to compute the speed at which the particle would reach the COG vertex. At last, events with a speed ranging from 0.25 to 0.4 m/ns can be rejected.

RTVeto : The RTVeto is based on the assumption that incoming atmospheric muons will trigger some DOMs before entering the DeepCore volume. The aim of this filter is to reject the events caused by these muons. The algorithm used considers the radial distance (R) and the time (T) in order to find clusters of hits. The RTVeto will notify the largest cluster of hits found with the pulse series. Since muons are expected to produce larger clusters than tracks induced by neutrinos, a cut based on the cluster size can be deduced to veto incoming muons.

ConeCut : This cut uses the fact that the Cherenkov light produced by muons is emitted with a cone pattern. Once the track is reconstructed, a cone is placed with its tip at the interaction vertex of the event and its axis along the track direction. The first step of this cut is to determine the pulses in ConeCutPulses. This pulses are selected to be InIcePulses within the cone of given opening angle, considering a time offset 500 ns and a time window of 1000 ns. Secondly, the number of hit DOMs of the ConeCutPulses is calculated. The number of channel (NCH), that is to say the number of hit DOMs, must be optimized with respect to the opening angle of the cone. The optimal cut efficiency was found for opening angle between 20° and 30°.

RZCut : The RZCut is a two-dimensional technique to spot muons entering the detector volume based on the radial distance, r, of the track vertex to the central string and the vertical coordinate, z of the first hit DOM. The position of the vertex is computed using a reconstruction algorithm from the noise-cleaned event hits. The distance r is defined as $r = \sqrt{x^2 + y^2}$, with x and y being the horizontal coordinates of the vertex. From these coordinates, a two-dimensional r-z map is constructed with the signal fraction contained in each bin. This signal fraction is defined as $f_s/(f_s + f_{bg})$, with f_s and f_{bg} being respectively the signal and background PDFs.

LHVeto : The aim of the LHVeto is to reject incoming muons that have not been identified by the previously applied veto techniques. Some of these muons are producing very few hits in the veto region that are too far apart to be cut out by the other techniques. This veto considers all the hits contained in a cylinder of given radius around the initial reconstructed track. The log likelihood (llh) value of the track is calculated by using only those pulses. This technique establishes how likely the pulses are to be associated with a muon track. Indeed, if the hits are somehow connected to the track, the likelihood value is affected. Hits produced by a muon tend to have highest llh values than random distributed noise hits.

4.3 ANTARES

ANTARES, which stands for Astronomy with a Neutrino Telescope and Abyss Environmental RESearch, is an underwater Cherenkov detector. This neutrino observatory is located in the deep Mediterranean sea, about 40 km from Toulon at the coordinates 42°48'N, 6°10'E [**ANTARES_location**]. ANTARES consists of 12 strings of 350 meters length each, spread over a surface of 0.1 km^2 at a depth of about 2475 m [7] with a distance of 70 meters between each string. These flexible strings are anchored to the seabed and remain in vertical position by means of buoys. Each string holds 25 storey of 3 Optical Module (OM) seperated by 14.5 meters, making a total of 1000 OMs. A schematic view of the detector can be seen in Fig. 4.5. The movements of the strings are monitored using a system of hydrophones and compasses installed within the detector volume.

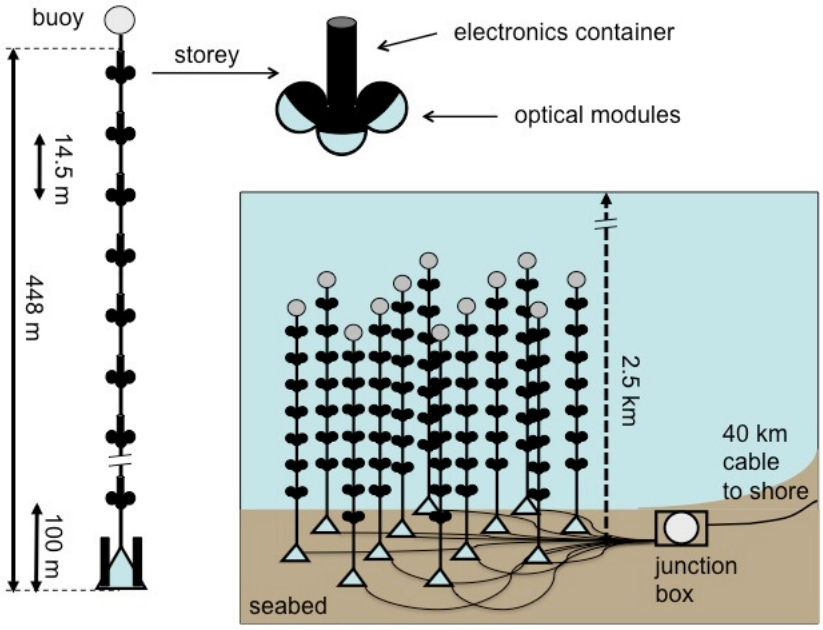

FIGURE 4.4: Schematique view of the ANTARES neutrinos telescope. It contain 885 PMTs distributed along 12 lines anchored at the sea bottom [7].

The optical modules are composed of a photomultiplier tube, various sensors and the associated electronics enclosed in glass spheres (OMs). The sphere as a diameter of 43 cm and a thickness of 1.5 cm is resistant up to a pressure of 700 bars. In a storey, each module is disposed such as the axis of the photomultiplier tube is 45° below the horizontal. This setting offers an high efficiency for the detection of light coming from the South hemisphere.

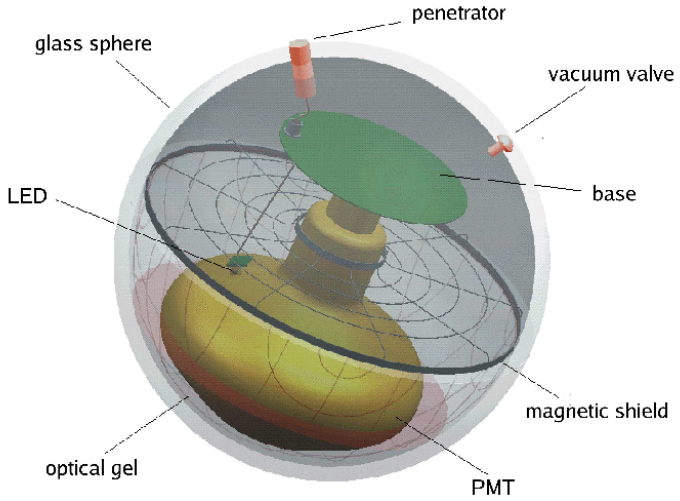

FIGURE 4.5: Schematique drawing of an optical module (OM) used in the ANTARES neutrinos telescope. Each OM contained a PMT as well as associated electronics [7].

The Cherenkov photons detected by the OMs, which are called hits, are processed by a data acquisition system. The recorded hits are transferred to the junction box through the line from the Local Control Module (LCM) contained in the storeys. The junction box acts as a link between the detector and the observation station located in La Syne-sur-mer.

Two types of reconstruction are used in ANTARES, depending on the deposited energy of the events. The single line reconstruction, also called BBFit, is used for events below 100 GeV/c^2 while the multi-line reconstruction (AAFit) is more appropriate for energies over 100 GeV/c^2.

4.4 Light Propagation in the Detectors

Neutrino interactions create secondary charged particles emitting Cherenkov radiation while travelling through the detector medium. These Cherenkov photons will behave differently in IceCube and ANTARES due to the different detector medium, as we will see in the next section. This behaviour will, among others, explain the sensitivity differences that will be observed between the two detectors during our analysis.

4.4.1 IceCube

As already explained, IceCube indirectly searches for neutrinos by detecting the Cherenkov light produced through the interaction of charged leptons induced from the neutrinos interaction with nuclei in the detector volume. Since the lepton and thus the neutrino direction is reconstructed using the photon arrival times at the PMTs, it is crucial to understand the propagation of the Cherenkov photons from their emission point to the receiving sensor. These photons are subject to absorption and scattering while travelling through the South Pole ice. To describe the effects of absorption and scattering of photons we can introduce the effective scattering coefficient, b_e, and the absorption

coefficient, a_{dust}. These coefficients are defined respectively as the inverse of the scattering length, $(1/\lambda_{scatt})$, and the inverse of the absorption length, $(1/\lambda_{abs})$ [35]. These parameters have been measured and are monitored using *flasher run datasets*, which are generated by sending photons from the LED located in one DOM and detecting this light with other surrounding DOMs.

The most commonly used model in IceCube for this purpose is SPICE-MIE, a six-parameter ice model based on a sophisticated parametrization of Mie scattering [18]. This model describes the ice using the effective scatteting coefficient and the absorption coefficient related to scattering and absorption for light of 400nm wavelength, for which IceCube DOMs are the most efficient. This model also use six global parameters (α, κ, A, B, D and E), which are fitted to the flasher run data as described in details in [11]. The scattering and absorption coefficients are depth, pressure and temperature dependent. Impurities of the ice, like the dust layer, also degrade the optical properties of the ice. For depth going from 1300 m to 2600 m, the scattering absorption and profile are listed in 10 meters steps, which is smaller than the vertical DOM spacing.

The model shows that ice is clearer at the bottom of the detector and that the ice has a layered structure. This layer structure is due to the fact that the South Pole ice has been formed by accumulation of snow over at least 165 thousands years [21]. Because of the pressure, the air bubbles content decreases with depth [**bubble**]. This is the main reason why IceCube DOMs are deployed at depths between 1450 m to 2450 m. However, at depths between 1950 m and 2150 m the scattering and absorption are a factor 4 above the average due to a higher concentration of dust particles, referred to as the *dust layer*. **The ice properties ...**

4.4.2 ANTARES

On a similar note, a proper understanding of the photon propagation in the ANTARES detector is required. Namely, understanding the effects of absorption and scattering on Cherenkov light in the sea water. The scattering and absorption of these photons in sea water are described mainly by the effective scattering length, λ^{eff}_{scatt}, and the absorption length, λ_{abs}. The effective scattering length is related to the normal scattering length, λ_{scatt}, and the average cosine of the total scattering angular distribution, $\langle cos\theta \rangle$ through the equation

$$\lambda^{eff}_{scatt} = \frac{\lambda_{scatt}}{1 - \langle cos\theta \rangle} \, . \tag{4.3}$$

The absorption and scattering length are monitored using the optical beacons designed for the calibration. The absorption length can induce an error on the effective area of the telescope, up to 5% at the highest energies ($\sim 10^7$ GeV) to 15% for the lowest energies ($\sim 10^2$ GeV). However, ... the effective scattering length mostly alter the angular resolution with an uncertainty factor of 0.05° to 0.1°.

4.5 Expected Background

The main background sources for both detectors consist of atmospheric muons and neutrinos. These particles are secondary particles produced in the interaction of cosmic rays with higher layers of the atmosphere. The primary cosmic rays consist mainly

of protons and helium nuclei but heavier ions as well as non-baryonic component can be found. These primary particles interact with the nuclei of the atmosphere and create hadronic and electromagnetic air showers. The secondary particles then created are highly energetic and relativistic. They will also interact or decay into ligther particles, creating among others muons and neutrinos. Atmospheric muons trigger the detectors more than 6 orders of magnitude more often than atmospheric neutrinos.

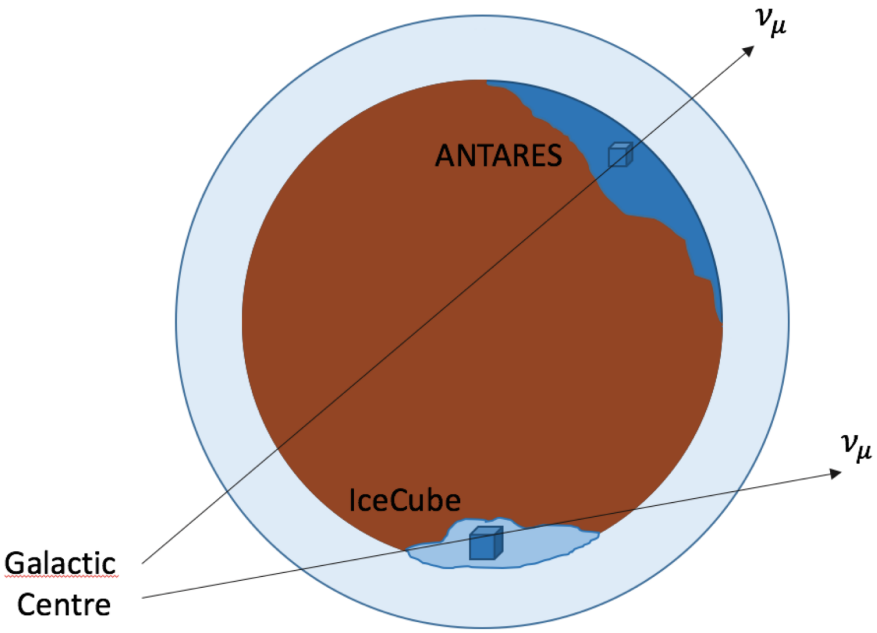

FIGURE 4.6: Schematic view of both ANTARES and IceCube location. The Galactic Center is located in the southern sky.

Atmospheric muons are created in decays of mesons, e.g. pions and kaons, themselves produced by the interaction of cosmic rays in the atmosphere. Due to their high energy and their relatively long lifetime, these muons are able to reach the surface of the Earth as well as the ANTARES and IceCube detectors. However, muons have a limited mean free path length in matter and their maximal penetration distance is about 20 km [**PDF**]. This means that for up-going directions, the Earth acts as a shield against atmospheric muons. As a consequence, declination corresponding to angles between $0° - 90°$ are less muon background dominated in the IceCube detector. Despite this advantage, IceCube selects up-going as well as down-going tracks. On the contrary, ANTARES only consider up-going track in its detector volume. For the ANTARES telescope, declination below -47° are favoured since they are always below the horizon of the detector. Declination between -47° and 47° are below the horizon for part of the sidereal day. Since the Galactic Centre is located in the southern hemisphere, with a declination of -29.01°, IceCube observes the GC with a background dominated by atmospheric muons. Despite its smaller scale, ANTARES has a privileged view of the Galactic Centre with a visibility of 75%, i.e. the percentage of time when the GC can be observed below the horizon. ANTARES can use the Earth to block the main contribution of the atmospheric background and therefore no veto is necessary. A two-dimensional map of both detectors horizon can be found in fig. 4.7

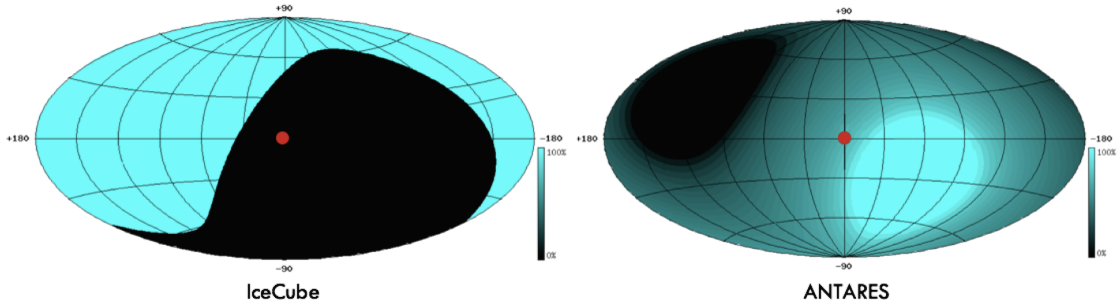

FIGURE 4.7: Two-dimensional view of the horizon for both the IceCube (left) and ANTARES (right) telescopes. The red dots representing the position of the Galactic Centre.

Atmospheric neutrinos, which are also part of the background, are produced in the decays of pions, kaons and muons. By contrast with muons, only neutrinos with very hight energies, i.e. around 1PeV, can be vetoed by the Earth. For analysis below this energy, atmospheric neutrinos from all directions constitute a relevant background.

Since ANTARES is located in the Mediterranean sea, background due to the environment also have to be consider. Bioluminescence, which is the light produced by micro-organisms living in the water, is one of them. Hits produced by bioluminescence can be wrongly selected as being part of particle events and interfere with the events reconstruction. Bioluminescence is a seasonal phenomenon and reaches its maximum in spring and can cause the ANTARES detector to be put into a reduce high voltage mode in order to avoid damages due to the high of photon hits.

Chapter 5

ANTARES and IceCube Event Selection

At trigger level both ANTARES and IceCube event rate is dominated by the large contribution of atmospheric muons. The goal of event selection is to reduce as much as possible the existing background while filtering out a possible neutrino signal. Each event selection depends on the experimental needs as some analysis will make use of high quality track reconstructed events, while others will privilege good energy reconstructed events. In this analysis we will make use of event samples already available in ANTARES and IceCube which were optimized for search of DM annihilation from the Galactic Center.

The general approach for event selections is to use neutrino simulation weighted according to the spectrum of dark matter annihilation signal (for a given mass and annihilation channel) and Monte Carlo simulation or real data to describe the background.

In this analysis no data selection was shared among collaboration, only the final event distributions were shared in order to produce the projected sensitivities calculated in this study. A final exchange of the real data will happen after the agreement of both collaboration to perform the analysis.

Given the different scales and location of both experiments, their event selections rely ...

5.1 The IceCube Data Selection

The study has been conducted with the data sample used for the IC86 low energy Galactic Centre analysis [**IC86**]. This analysis is composed of three years of data taken with the IceCube 86-strings configuration from the 15th of May 2012 to 18th of May 2015. Multiple event selections and cuts have been applied on the events using a series of filters starting at level2. This level is composed of the events passing any IceCube filter and are provided by the IceCube Collaboration. The details of this event selection can be found in ref. [**IceCube_selection**].

5.1.1 Simulation datasets

In order to reduce the amount background from the data while keeping the neutrino signal, different Monte Carlo simulations are needed to assert the background rejection and the signal efficiencies. Background is composed of atmospheric muons and atmospheric neutrinos and for each of these components a dedicated simulation is used. In this study however only atmospheric neutrino simulation is shown, as data is used

Cut	Level 3 selection criteria
I	Event passed the DeepCore filter
II	Event passed the pulsed time containment veto
III	Event passed the detector top veto
IV	$N_{Str} > 3$
V	NCh > 10

TABLE 5.1: Level 3 cuts and passing conditions for the Galactic Centre low energy analysis

as the overall background estimator. For low energy neutrinos simulations the Genie software was used. Genie is a program used to simulates atmospheric neutrinos of all-flavour, as well as signal neutrinos [24]. The atmospheric neutrino flux is determined by using the Honda parametrization [**Honda**]. The Genie event generator is used for the simulation of low energies neutrinos, ranging from MeV to a few GeV.

In order to mimic the expected signal, the Genie datasets are weighted according to the equation **??**. This weight is dependent of the direction and the energy of the neutrino. The neutrino energy spectrum per annihilating WIMP pair for different annihilation channel of 100 GeV WIMPs to ν_μ as a function of the energy is represent in fig. **??**.

$$w = \frac{1}{2}\frac{\langle\sigma_a\nu\rangle}{4\pi\, m_\chi^2}\frac{w_{OW}}{N_{events}}\, J_\Psi \frac{\mathrm{d}N}{\mathrm{d}E} \tag{5.1}$$

where $\langle\sigma_a\nu\rangle$ is the annihilation cross section that this analysis is trying to constrain. J_Ψ is the J-factor as defined by equation 2.5, m_χ is the mass of the WIMP and w_{OW} is OneWeight, which is the weight corresponding to one particle per GeV cm2 sr. The J-factor distribution in regards to the opening angle to the Galactic Centre, Ψ, can be found in fig. **??**.

5.1.2 Level 3

The first event selection consist of taking only events passing the DeepCore filter, *i.e.* events starting in the DeepCore fiducial volume as describe in section 4.2. The aim of this filter is to reject atmospheric muons by analysing the hit DOMs inside and outside DeepCore separately. In order to reduce the muon background, events must also pass the detector top veto. A cut was also made on the number of DOMs hit (NCh > 10) as well as on the number of hit strings ($N_{Str} > 3$). Indeed, events with few hit DOMs and string usually result in badly reconstructed events. Since this analysis is focusing on the region of the sky where the GC is located, these events are not contributing to the sensitivity of the analysis.

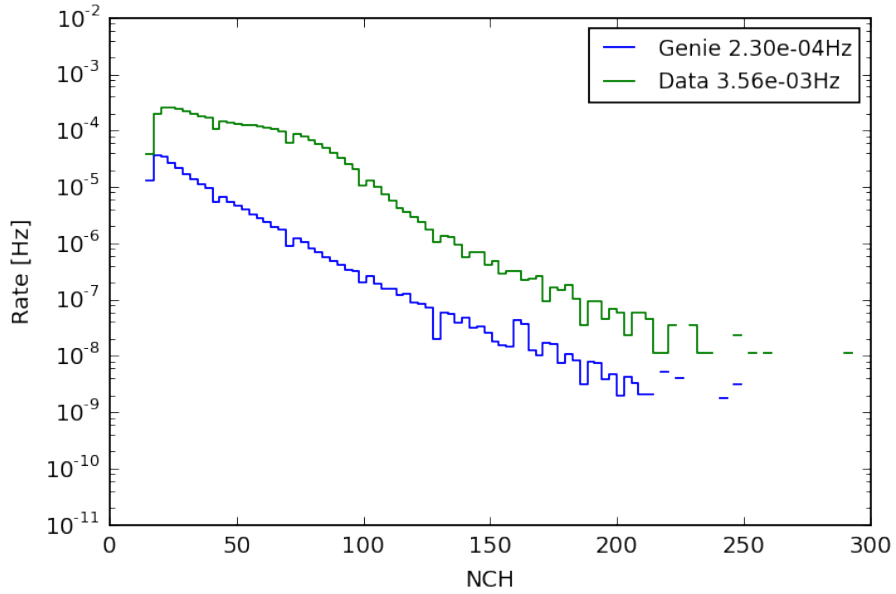

FIGURE 5.1: Distribution of the number of DOMs hit for for data (green line) and Genie simulation for atmospheric neutrinos (blue line). The difference between the two lines is due to atmospheric muons. Only events with a number of channel above 10 were selected.

5.1.3 Level 4

The level 4 selection focuses on well reconstructed events contained in the DeepCore fiducial volume. The passing condition on the Level 4 selection are listed in table 5.2. The first two cuts ensure that badly reconstructed events are removed from the data sample. The third cut reduce the amount of data by selecting only event located in a window of 40° around the Galactic Centre (GC), *i.e.* $40° < \Theta_{zen} < 80°$ ($\pm 20°$ around GC). This selection is made knowing that signal is expected from this narrow zenith band centred on the Galactic Centre ($61°$ in zenith or $29°$ in declination). On the other hand, atmospheric muons tend to penetrate the detector from top to bottom, hitting mostly DOMs along the vertical detector axis z. In this sense, the fourth cut is rejecting events with spread in the z-coordinate of hit DOMs of more than 80 metres. The cut V select events that are contained in DeepCore by requiring that the finite reconstruction track length is smaller than 600 m, which roughly correspond to the diagonal size of the DeepCore sub-detector. Furthermore, only event starting in the DeepCore fiducial volume are selected by requiring that the vertex starting position should not be further away from the detector vertical centre axis than 250 m, $r_{FR} < 250m$. The most effective cut applied at this level is the RTVeto described in section 4.2.2. The RTVeto cut is set at a cluster size ≥ 3 which means that $\sim 81\%$ of the background will be removed while $\sim 93\%$ of the signal is kept.

Cut	Level 4 selection criteria
I	$\sigma_{par} < 13°$
II	$r_{llh} < 11$
III	$40° < \Theta_{zen} < 80°$ ($\pm 20°$ around GC)
IV	$\sigma_z < 80$m
	$\sigma_z < 250$m
	$\sigma_z < 600$m
V	Finite reconstruction tracklLenght $L_{FR} < 600m$
VI	Finite reconstruction radial $r_{FR} < 250m$
VII	Event passed the RTVeto

TABLE 5.2: Level 4 cuts and passing conditions for the Galactic centre low energy analysis

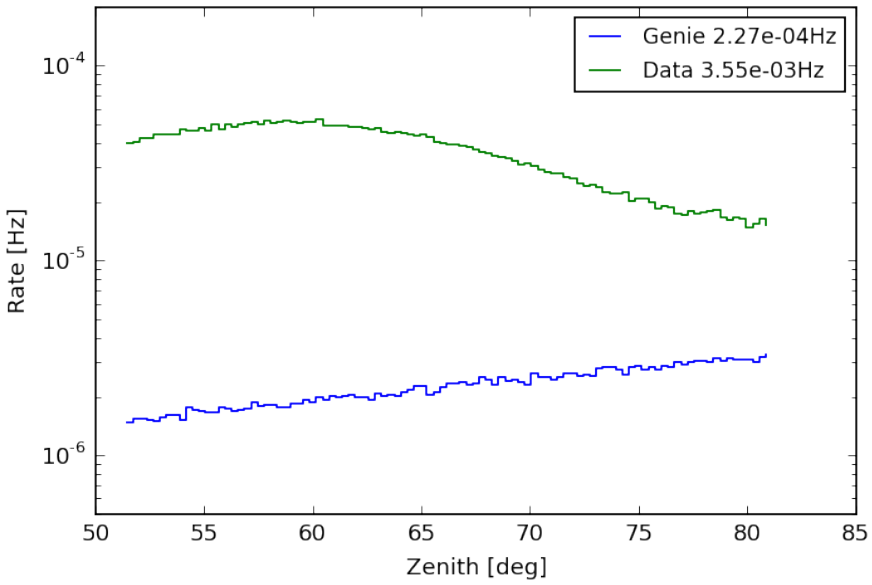

FIGURE 5.2: Zenith distribution of data (green) and the Genie neutrino simulation (blue). A cut was applied on the zenith, selecting only events with zenith between 50° and 80°. At this level, data is still dominated by atmospheric muons.

5.1.4 Level 5

The aim of level 5 cuts is to get rid of atmospheric muons that still dominated the data at level 4. The passing conditions for Level 5 are listed in the table 5.3. The cut I restricts the zenith angle band such as only event from $-10°$ to $20°$ around Galactic Centre are selected. As the majority of atmospheric muons have a reconstructed zenith angle smaller than the position of the GC, restricting the zenith angle band reduce the background rate by 27% while the signal efficiency is only altered by 4%. The most effective cut applied at this level is the RZCut which reject 62% of the data and keep 91% of the signal from level 4. The RZCut is a simple cut in the in the 2D space of the radial distance r from the centre string and the position z of the first hit DOM.

Deep events with radial distance to the detector centre r $>$ 160 and first hit DOM z position above -300 metres were rejected. Likewise, shallow events with z above - 300 metres and their radial distance to 36^{th} string above 2.333 r + 80 m were excluded [23]. As explained in the section 4.2.2, the LHVeto consist of calculating the likelihood of a track given a track reconstruction by using the pulses inside the veto region and contained in a cylinder around this track. This analysis evaluated the likelihood for three different cylinder radii = 250, 300 and 350 metres. The last cut applied was the ConeCut with a cone half opening angle of 20°. Only events with less than 2 hits found inside the cone were kept.

Cut	Level 5 selection criteria
I	$50° < \Theta_{zen} < 80°$ ($-10°$ to 20° around GC)
II	ConeCut < 2 hits
III	LHVeto(250m) $\geq$ 18
IV	LHVeto(300m) $\geq$ 11
V	LHVeto(350m) $\geq$ 6.8
VI	Event passed the RZCut

TABLE 5.3: Level 5 cuts and passing conditions for the Galactic Centre low energy analysis

5.1.5 Level 6 (BDT applied)

The Boosted Decision Tree (BDT) selection is the final cut applied on the sample. BDTs are use to evaluate the signalness of an event, denoted as the BDT score. Usually, BDT score range from -1 (background) to 1 (signal), *i.e.* the more the BDT score is close to one the more the event is signal-like. To determine the BDT score of an event, a signal and a background event sample (with the same set of event property variables defined for both samples) are used to train the BDT. This process creates a binary cut decision tree based on these variables. After the creation of the decision tree, the real data sample is passed in the BDT, which give us the BDT score. For this analysis, the BDT was trained on a 100 GeV/c^2 mass dark matter channel annihilating through W^+W^- as signal, and data as background. The optimised cut on the BDT score for the signal hypothesis is calculated using the sensitivity for different BDT cut values. The variables used in the final BDT are listed in table **??**. The optimized BDT cut applied on the data consist of a selection of BDT score over 0.25.

5.2 The ANTARES Data selection

The data selection used for this analysis is the same as in the search for dark matter in the Milky Way using 9 years of data of the ANTARES neutrino telescope [**ANT_9years**]. The data sample considered is composed of events recorded from 2007 to 2015, which corresponds to a total lifetime of 2102 days. Only neutrinos producing muons inside or around the detector are considered.

In order to reject events wrongly reconstructed as up-going muons, cuts on the reconstruction quality parameters (Q, Λ) and the angular error (β) were applied.

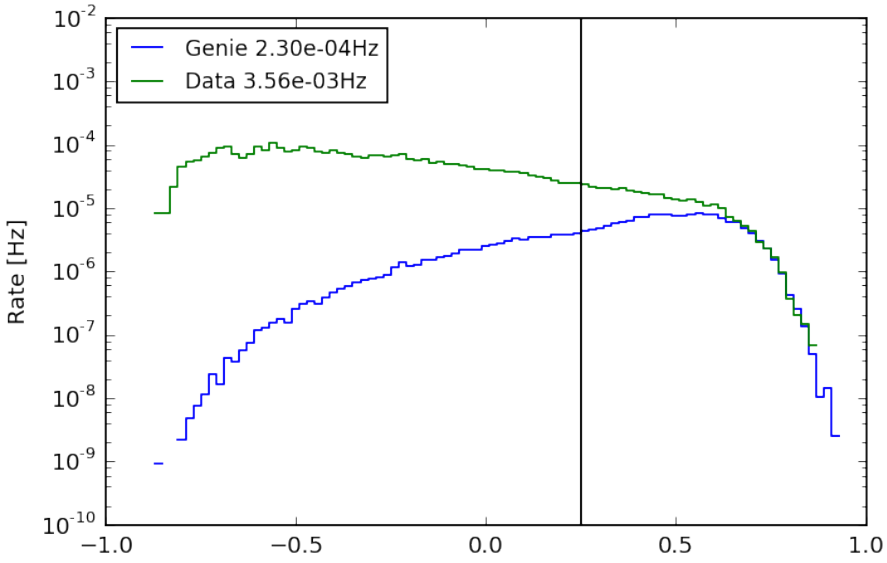

FIGURE 5.3: BDT score distribution for the IC86 GC analysis. The BDT was applied of data (green) and the Genie neutrino simulation (blue). The black line represents the optimised BDT cut and has a value of 0.25.

5.2.1 Reconstruction

Two types of track reconstruction are used by the ANTARES collaboration. The single-line reconstruction used for lower energies is called the BBFit [**BBfit**], while the multi-line reconstruction is known as the AAFit [**AAfit**]. For our analysis, we considered the AAFit for WIMP masses over 200 GeV/c^2 and the BBFit below this mass. Details of the two reconstruction can be found in ref. [**AAfit**].

5.2.2 Simulation

Just as for the IceCube simulated signal sample, we need to weight the ANTARES signal simulation in order to obtain the simulated signal of neutrinos coming from dark matter annihilation. The weight is given for each WIMP masses annihilating through a specific decay channel given a halo model.

$$\text{Weight} = \frac{1}{2}\frac{1}{4\pi\, m_\chi^2}\,\mathcal{A}\,J_\Psi\,\phi_\nu \tag{5.2}$$

where m_χ is the WIMP mass, ϕ_ν is the integrated neutrino flux, $\mathcal{A}$ is the acceptance and J_Ψ is the integrated J-factor.

For the background, atmospheric muons and neutrinos were simulated using the standard ANTARES simulation algorithm. The energy range considered is ranging from 10 GeV/c^2 to 100 TeV/c^2. This simulation were used in order to calculate the detector resolution and the acceptance, cf. section 5.2.3.

5.2.3 Acceptance

The acceptance is a measure of the sensitivity to a signal having a specific spectrum. The acceptance, $\mathcal{A}$, linked the number of signal events detected, μ_d, to the neutrino flux, ϕ_ν, by the equation

$$\phi_{\nu_\mu} \cdot \mathcal{A} = \mu_d \tag{5.3}$$

The effective area, A_{eff}, is needed in order to determine the acceptance. The effective area represent the area of a perfect detector, that is to say a detector configuration with a 100 % detection efficiency which would produce the same event rate as the detector. The effective area can be calculated using the following equation

$$\int_{E_th}^{\infty} \frac{\mathrm{d}\phi_{\nu_\mu}(E_{\nu_\mu})}{\mathrm{d}E_{\nu_\mu}} A_{eff}(E_{\nu_\mu})\,\mathrm{d}E_{\nu_\mu} = \mu_d \ , \tag{5.4}$$

with E_ν being the energy of the neutrino and E_th the energy threshold of the ANTARES telescope. The neutrinos flux being unknown, the effective area has to be determined from the signal simulation. Unlike the effective area, the acceptance has a dependence on the signal neutrinos spectrum at Earth. The acceptance is determined by the convolution of the neutrino effective area with the energy spectrum corresponding to a given WIMP mass. This is done according to the following equation :

$$\mathcal{A}(m_\chi) = \int A_{eff}(E_{\nu_\mu}) \frac{\mathrm{d}N_{\nu_\mu}}{\mathrm{d}E_{\nu_\mu}}\bigg|_{ch,m_\chi} \mathrm{d}E_{\nu_\mu} + \int A_{eff}(E_{\bar{\nu}_\mu}) \frac{\mathrm{d}N_{\bar{\nu}_\mu}}{\mathrm{d}E_{\bar{\nu}_\mu}}\bigg|_{ch,m_\chi} \mathrm{d}E_{\bar{\nu}_\mu} \tag{5.5}$$

with $A_{eff}(E_{\nu_\mu})$ or $A_{eff}(E_{\bar{\nu}_\mu})$ being the effective area for the muon neutrino energy or the muon anti-neutrino energy, $\mathrm{d}N_{\nu_\mu}$ the signal neutrino spectrum at the detector for one particular annihilation channel (ch) and WIMP mass (m_χ).

The acceptance for each annihilation channels used in this analysis is represented in fig. **??**. The acceptance was computed for both the AAFit (continuous line) and the BBFit (dashed line).

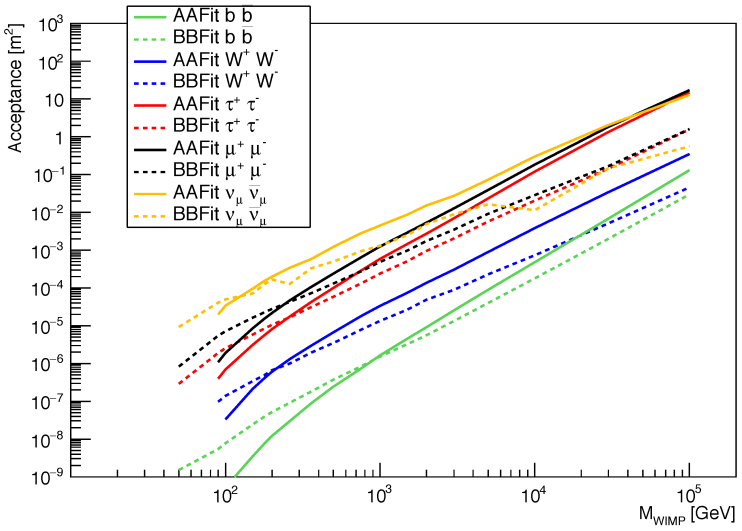

FIGURE 5.4: Acceptance computed for each annihilation channel used in our analysis ($b\bar{b}$, W^+W^-, $\nu_\mu\bar{\nu_\mu}$, $\mu\bar{\mu}$, $\tau\bar{\tau}$). The acceptance is given for both the AAFit (continuous line) and BBFit (dashed line). Plot taken from **[plot_acceptance]**

Chapter 6

Analysis Method

In this chapter we will describe the statistical method used for this analysis. This analysis applies a binned maximum likelihood method using a two component model. The null hypothesis states that data can be described by only background events, while the testing hypothesis describes data as a combination of background and signal events. In order to build both hypothesis we need to construct both the background and signal probability density distributions (PDFs). Only the directional information is used in this analysis. Signal is expected to produce an excess in the direction of the Galactic Center, while the background is will have only a declination dependence but will be uniform in right ascension. The excess of the signal will depend on the halo model, annihilation channel, WIMPs mass, etc. and it will be different for each detector.

6.1 Analysis Overview

As mentioned earlier, this analysis consists in an indirect search for dark matter annihilation in the Galactic Centre using two neutrino detectors, IceCube and ANTARES. The aim of this combined search is to, if no detection is made, set limits on the thermally average self-annihilation cross-section of dark matter. As exposed in section 2.2.2, we will consider dark matter to be composed of WIMPs. Various WIMP masses are considered in this work, ranging from ranging from 50 to 1000 GeV/c^2. Five different WIMP annihilation channels are also taken into account. The halo density profile used in this analysis is the Navaro-Frenk-White (NFW) profile, as mentioned in section 2.4. The table 6.1 summarised the different signal hypotheses used for our analysis.

6.2 Likelihood Method

The binned likelihood method used in this analysis is defined as

$$\mathcal{L}(\mu) = \prod_{bin_i=bin_{min}}^{bin_{max}} \text{Poisson}\left(n_{obs}(bin_i)|n_{obs}^{tot}\, f(bin_i|\mu)\right) \ , \tag{6.1}$$

where the parameter to minimize, μ, is the ratio of the number of signal events over the total number of background events in the sample n_{obs}^{tot}. The method compares the observed number of events in a given bin i, $n_{obs}(bin_i)$, with the expectations, n_{obs}^{tot}, $f(bin_i|\mu)$, where

$$f(bin_i|\mu) = \mu\, f_s(bin_i) + (1-\mu)\, f_{bg} \ , \tag{6.2}$$

TABLE 6.1: Table of the caracteristics of WIMP particles tested in our analysis. Several WIMP masses and annihilation channels were considered.

	IceCube	**ANTARES**	**Combined Search**
WIMP Halo Profile	NFW Halo Profile		
WIMP Masses	10 GeV 20 GeV 30 GeV 40 GeV 50 GeV 65 GeV 100 GeV 130 GeV 200 GeV 300 GeV 400 GeV 500 GeV 1000 GeV	50 GeV 65 GeV 100 GeV 130 GeV 200 GeV 300 GeV 400 GeV 500 GeV 1000 GeV	
WIMP Annihilation Channels	$\chi\chi \to b\bar{b}$ $\chi\chi \to \mu\bar{\mu}$ $\chi\chi \to \nu_\mu\bar{\nu}_\mu$ $\chi\chi \to \tau\bar{\tau}$ $\chi\chi \to W^+W^-$		

is the fraction of events in the bin i, with f_s and f_{bg} being the signal and the background density distributions. In the case of the IceCube sample, the background PDF is estimated by scrambling data in right ascension (each event was assigned a random RA value). As a result, signal contamination of the background can be accounted for by subtracting the right ascension scrambled signal PDF, $f_{scr.bg}$, from the background PDF

$$f_{bg} = (1+\mu)\, f_{scr.bg}(bin_i) - \mu\, f_{sc.sig}(bin_i)\ , \tag{6.3}$$

where $\mu \in [0,1]$ is the signal fraction in the total sample. Unlike the IceCube background PDF, the likelihood determination of the ANTARES sample does not take into account the signal contamination of the background.

In the case of the combined analysis, a combined likelihood has to be determined. Thus, both the IceCube signal contaminated likelihood and the ANTARES likelihood are combined in a single $\mathcal{L}_{comb}(\mu)$ defined as

$$\mathcal{L}_{comb}(\mu) = \prod_{k=0}^{2} \mathcal{L}_k(\mu_k)\ , \tag{6.4}$$

where $k = 0$ represents the ANTARES likelihood and $k = 1$ the IceCube likelihood. Each detector has a signal to background ratio given by $\mu_k = w_k \mu$ where the weight w_k is calculated by taking into account the relative expected number of signal events in each detector, and the relative number of background events in each sample.

6.3 Probability Density Function

This section is showing the probability density functions (PDFs) used for our combined analysis. The signal and background PDFs for both experiments, i.e. IceCube and ANTARES, are represented for all WIMP self-annihilation channels and for a specific WIMP mass.

6.3.1 IceCube

The signal and background PDFs were chosen to be two-dimensional distributions of the events in right ascension (RA) and declination (dec). The PDFs used are composed of 10 bins in right ascension and 12 bins in declination for a band covering [-2, 2] rad in declination and the full range in RA, i.e. [-2π, 2π]. So that a bin of these PDFs is 36° in right ascension and 19° in declination. The background PDF is filled with data scrambled in right ascension, so that it is uniform in RA. The background PDF is represented in figure 6.1.

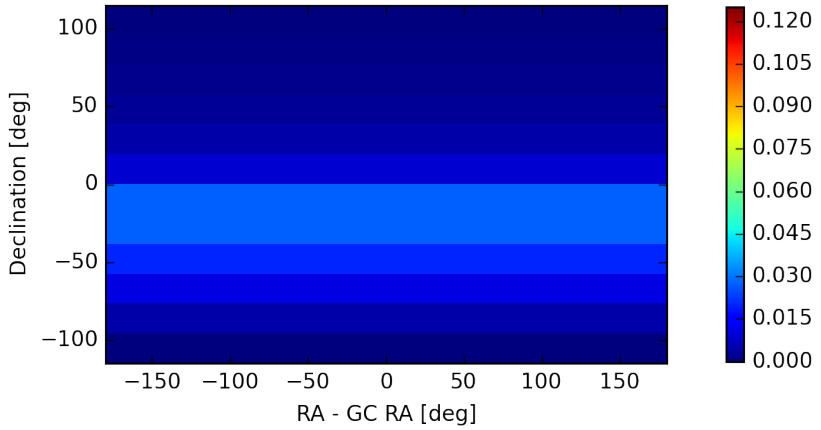

FIGURE 6.1: IceCube normalised background PDF for IC86 data taken from 2012 to 2015.

The signal PDFs have the same number of bins as the background PDF. These PDFs are filled with simulated signal for each WIMP masses and annihilation channels. The signal PDFs for all annihilation channels are listed below considering WIMP mass of 100 GeV/c^2.

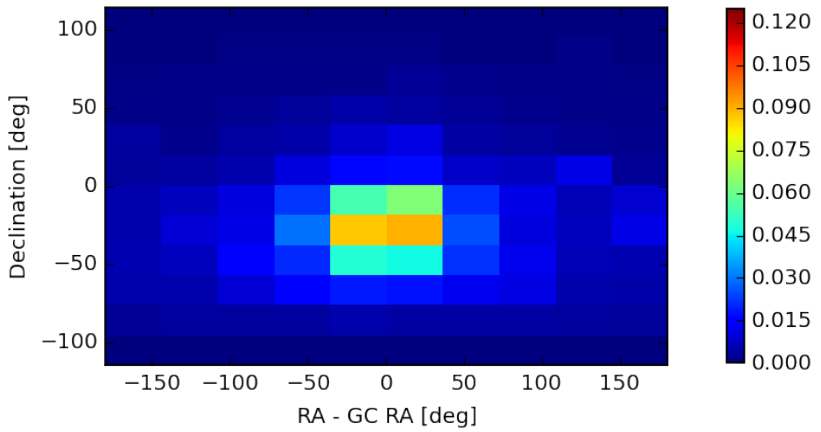

FIGURE 6.2: IceCube normalised signal PDF for WIMP mass of 100 GeV/c^2 annihilating respectively trough the $b\bar{b}$ channel.

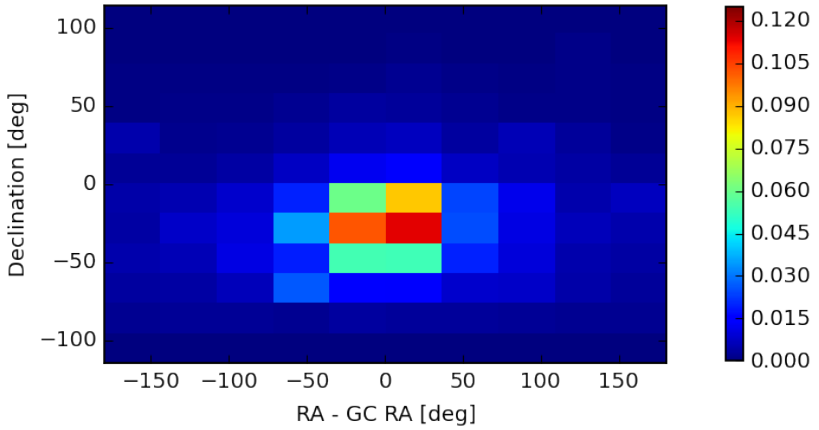

FIGURE 6.3: IceCube normalised signal PDF for WIMP mass of 100 GeV/c^2 annihilating respectively trough the W^+W^- channel.

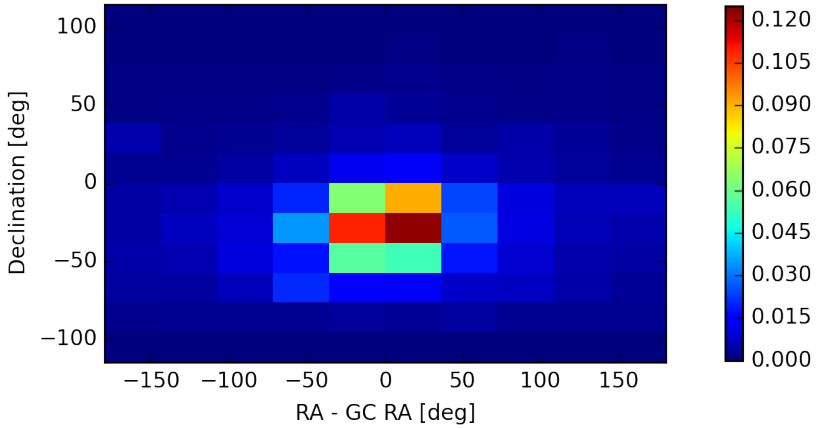

FIGURE 6.4: IceCube normalised signal PDF for WIMP mass of 100 GeV/c^2 annihilating respectively trough the $\tau\bar{\tau}$ channel.

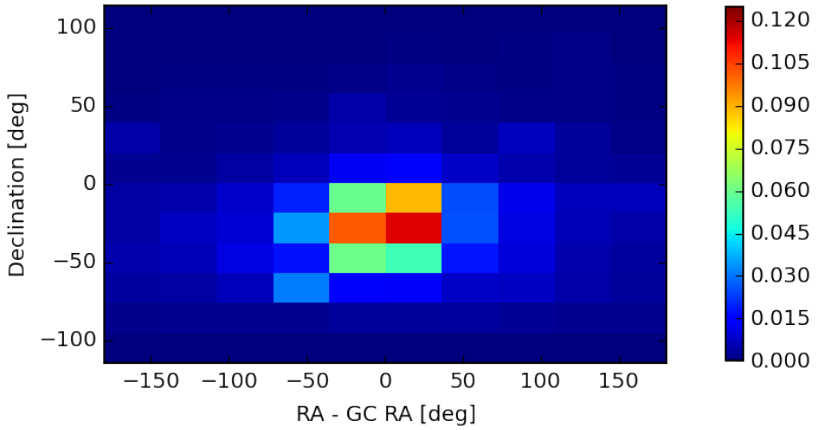

FIGURE 6.5: IceCube normalised signal PDF for WIMP mass of 100 GeV/c^2 annihilating respectively trough the $\mu\bar{\mu}$ channel.

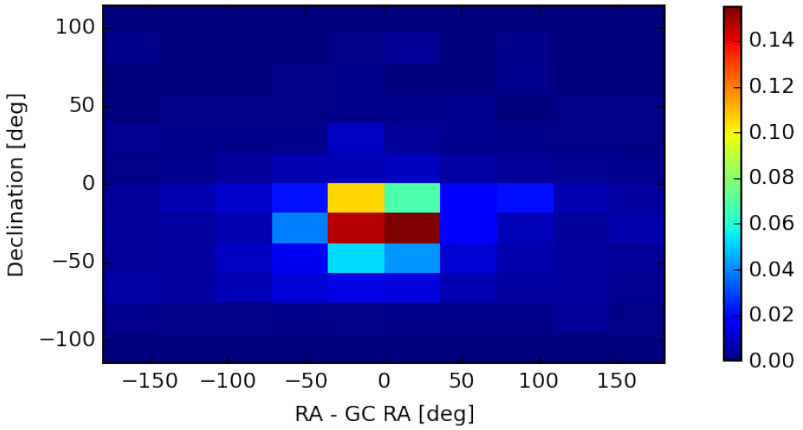

FIGURE 6.6: IceCube normalised signal PDFfor WIMP mass of 100 GeV/c^2 annihilating respectively trough the $\nu_\mu\bar{\nu}_\mu$ channel.

6.3.2 ANTARES

ANTARES PDFs are composed of 1-dimensional distributions of the opening angle to the Galactic Centre Ψ. For WIMP masses below or equal to 200 GeV/c^2, the background and signal PDFs are made using 100 bins with a range of -0.5 $\leq$ cos(Ψ) $\leq$ 0.5. For these WIMP masses, the single-line reconstruction was used. The PDF for a WIMP mass of 100 GeV/c^2 annihilating through the $\tau\bar{\tau}$, $b\bar{b}$, W^+W^-, $\mu\bar{\mu}$, and $\nu_\mu\bar{\nu}_\mu$ channel can be seen from fig. 6.9 to 6.12. For the background, the PDF using the BBFit can be found in Fig. 6.8.

For higher WIMP masses, the PDFs are composed of fewer bins, with 50 bins ranging from $0.5 \leq \log(\Psi) \leq 2$. The change from $cos(\Psi)$ to $textrmlog(\Psi)$ for the x-axis have no importance here since the code is comparing background and signal PDFs. So, since the signal and background PDFs are composed of the same number of bins, the x-axis can be changed without loosing consistence. This choice was motivated by the ANTARES collaboration in order to get the PDFs done quicker. The multi-line reconstruction, also called AAFit, is a better choice for these WIMP masses, so the PDFs were made using this reconstruction. The PDFs for 200 GeV/c^2 for all WIMP self-annihilation channels can be seen in fig. 6.14 to fig. 6.18. The corresponding background PDF is represented in fig. 6.13

6.4 Classical Confidence Intervals

The construction of these confidence intervals is done following Neyman's method [**Neyman**]. Classical confidence intervals allow the evaluation of the accurateness of a statistical parameter determination over a sample. A confidence interval (C.I.), $[\mu_1, \mu_2]$, is an interval in which the true parameter value, μ_{true}, will be contained with a certain probability, α, called the confidence level (C.L.)

$$P(\mu \in [\mu_1, \mu_2]) = \alpha \ . \tag{6.5}$$

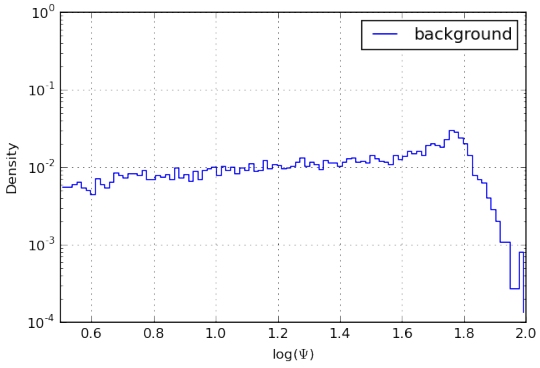

FIGURE 6.7: Normalized background PDF used for the ANTARES data using the BBFit reconstruction. The PDF is represented as a 1-dimensional histogram of the opening angle to the Galactic Centre Ψ.

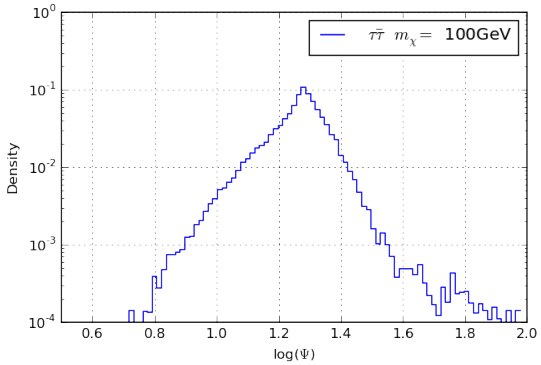

FIGURE 6.8: Normalized signal PDF for a WIMP mass of 100 GeV/c2 annihilating through the $\tau\bar{\tau}$ channel using the BBFit reconstruction.

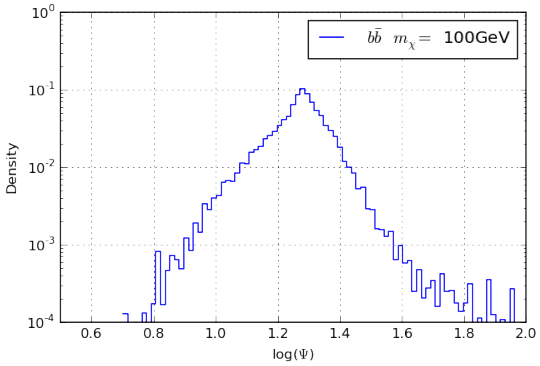

FIGURE 6.9: Normalized signal PDF for a WIMP mass of 100 GeV/c2 annihilating through the $b\bar{b}$ channel using the BBFit reconstruction.

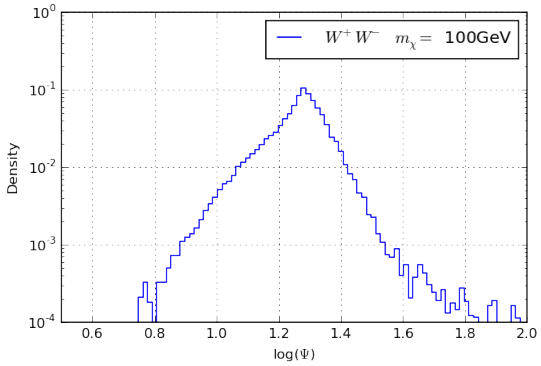

FIGURE 6.10: Normalized signal PDF for a WIMP mass of 100 GeV/c2 annihilating through the W^+W^- channel using the BBFit reconstruction.

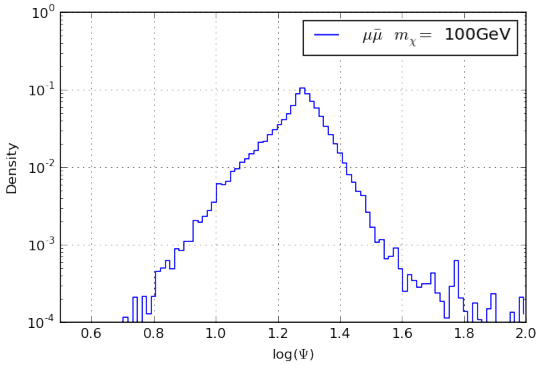

FIGURE 6.11: Normalized signal PDF for a WIMP mass of 100 GeV/c2 annihilating through the $\mu\bar{\mu}$ channel using the BBFit reconstruction.

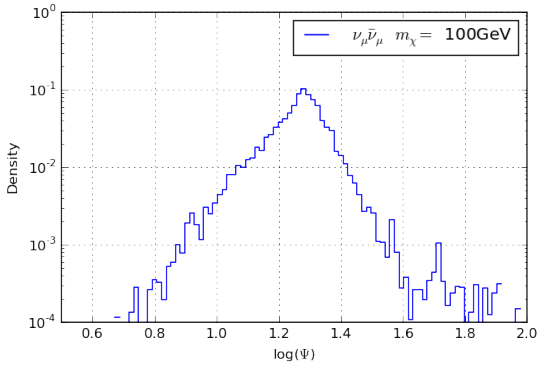

FIGURE 6.12: Normalized signal PDF for a WIMP mass of 100 GeV/c2 annihilating through the $\nu_\mu\bar{\nu}_\mu$ channel using the BBFit reconstruction.

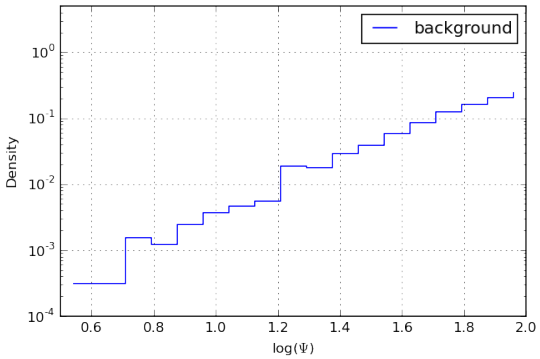

FIGURE 6.13: Normalized background PDF for the AAFit reconstruction. The PDF is represented as a 1-dimensional histogram of the opening angle to the Galactic Centre Ψ.

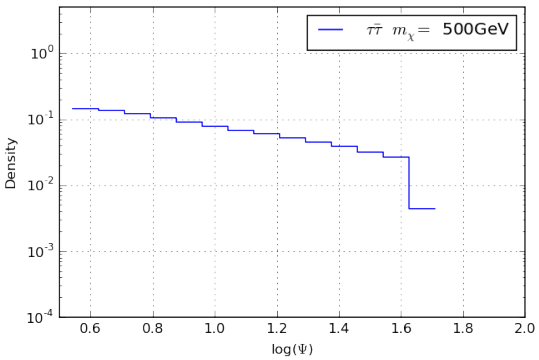

FIGURE 6.14: Normalized signal PDF for a WIMP mass of 100 GeV/c2 annihilating through the $\tau\bar{\tau}$ channel using the AAFit reconstruction.

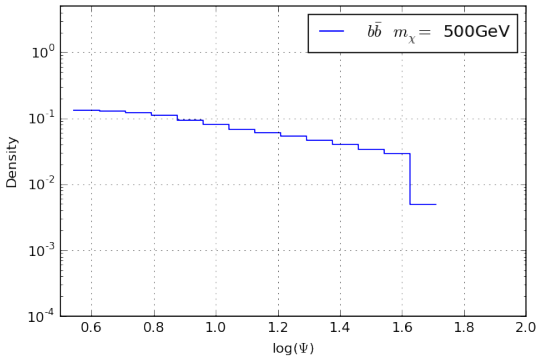

FIGURE 6.15: Normalized signal PDF for a WIMP mass of 100 GeV/c2 annihilating through the b channel using the AAFit reconstruction.

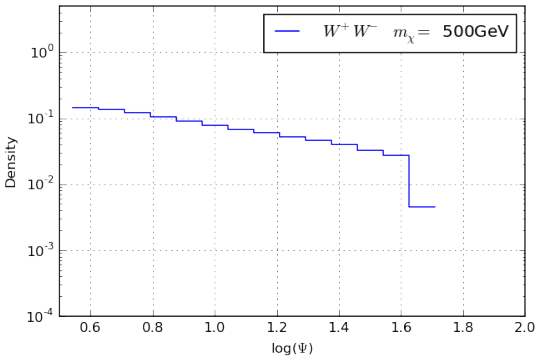

FIGURE 6.16: Normalized signal PDF for a WIMP mass of 100 GeV/c2 annihilating through the $W+W-$ channel using the AAFit reconstruction.

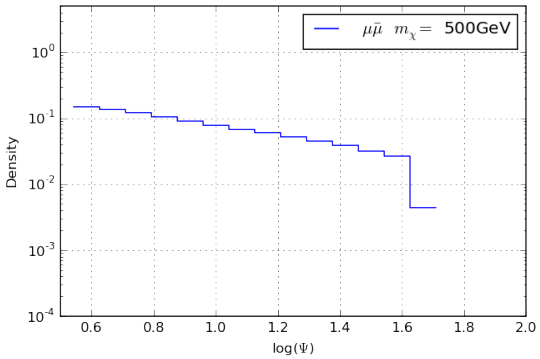

FIGURE 6.17: Normalized signal PDF for a WIMP mass of 100 GeV/c2 annihilating through the $\mu\bar{\mu}$ channel using the AAFit reconstruction.

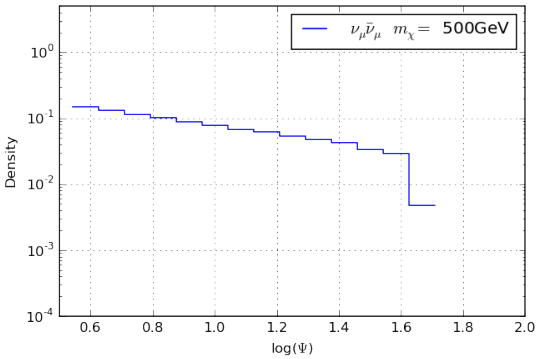

FIGURE 6.18: Normalized signal PDF for a WIMP mass of 100 GeV/c2 annihilating through the $\nu_\mu\bar{\nu}_\mu$ channel using the AAFit reconstruction.

This interval provides a lower and upper limit, respectively μ_1 and μ_2, for a given confidence level α. The values μ_1 and μ_2 are functions of the measured x. The equation 6.5 is true for every allowed μ, and in particular for the true value μ_t. If equation **??** is satisfied, than it is said that the interval cover μ for the given confidence level. On the contrary, if there is a value of μ such as $P(\mu \in [\mu_1, \mu_2]) < \alpha$, one can say there is "under-coverage" for that particular μ. The term "over-coverage" is used if the case $P(\mu \in [\mu_1, \mu_2]) > \alpha$ is encountered for a value of μ.

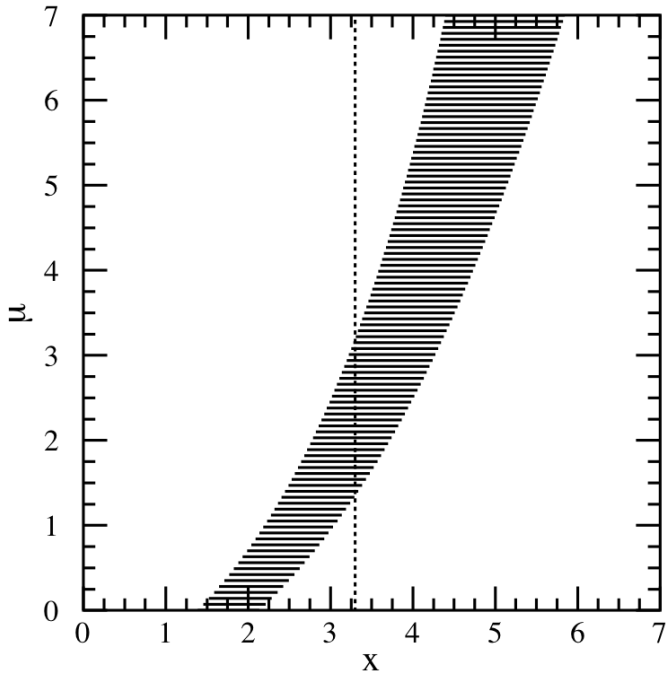

FIGURE 6.19: For each value of μ, an horizontal acceptance interval $[x_1, x_2]$ is drawn with $P(x \in [x_1, x_2] \,|\, \mu) = \alpha$. The confidence interval $[\mu_1, \mu_2]$ is given by the union of all μ values for which the corresponding acceptance interval is crossed by the dashed vertical line. This vertical line representing the value x_0 obtained upon performing an experiment to measure x. Figure taken from **[Feldman_cousins_paper]**.

The determination of the confidence intervals requires the construction of acceptance intervals, $[x_1, x2]$, such that

$$P(x \in [x_1, x_2] \,|\, \mu) = \alpha \; . \tag{6.6}$$

for each value of μ. These intervals are drawn, for each μ, as horizontal segments on the plot representing the parameter μ as function of the measured quantity x (cf. fig. 6.19).

In order to determine the values of x in $P(x|\mu)$ along the horizontal line for each μ, an arbitrary criteria is chosen. For the classical confidence interval construction, two choices were proposed by Neyman. The first condition to satisfy is

$$P(x < x_1 \,|\, \mu) = 1 - \alpha \,, \tag{6.7}$$

leading to the "upper confidence limits", which satisfy the condition $P(\mu > \mu_2) = 1 - \alpha$. The second choice is given by

$$P(x < x_1 \,|\, \mu) = P(x > x_2 \,|\, \mu) = (1 - \alpha)/2 \,, \tag{6.8}$$

and leads to the so-called "central confidence intervals" which satisfy $P(\mu < \mu_1) = P(\mu > \mu_2) = 1 - \alpha$.

When horizontal acceptance are drawn for every value of μ, Neyman's construction is completed. The next step in order to determine the confidence interval is to measure x and obtaining the value x_0 shown as a dashed vertical line on the fig. 6.19. The confidence interval $[\mu_1, \mu_2]$ is given by the union of all μ values for which the corresponding acceptance interval is intercepted by the dashed vertical line.

Two major issues can arise from Neyman's construction of confidence intervals. The first problem lies in the fact that one have to chose between this two conditions, i.e. upper confidence limits or central confidence intervals, prior to the measurement. This issue is known as the "flip-flopping" problem. Second, Neyman's construction can lead to unphysical confidence level. In order to avoid these two problems, Feldman and Cousins proposed a new method exposed in section 6.5.

6.5 Feldman-Cousins Method

The method proposed by Feldman and Cousins involves an ordering principle. The choice of the acceptance interval is based on likelihood ratio

$$R = \frac{P(x|\mu)}{P(x|\mu_{best})} \tag{6.9}$$

where $f(x, \mu)$ is the likelihood of μ given x and $fx, \mu_{best})$ is the value of μ maximising the likelihood for a given x.

Once the likelihood ratio R is determined, a rank is given to the x values with decreasing order of R. The x values are then added to the acceptance interval according to their rank until the sum of $P(x|\mu) \geqslant \alpha$. The same steps are repeated for every value of μ. A comparison between upper Limit and central intervals is conducted. In this way, the choice between the two types of interval is intrinsic.

All confidence intervals in our analysis were constructed using the Feldman-Cousins method [**Feldman_cousins**]. The method was already implemented for previous analysis and can be found in the MLSandbox [**MLSandbox**].

6.6 Results : Sensitivities

For both ANTARES and IceCube individual likelihoods or the combined likelihood, the best estimate of the signal fraction can be given by minimizing $-log\mathcal{L}_{IceCube}$, $-log\mathcal{L}_{ANTARES}$

or $-log\mathcal{L}_{comb}$ respectively. If this value is consistent with zero, the upper limit on the signal fraction, $\mu_{90\%}$, is estimated by determining the 90% confidence interval using the Feldman-Cousins approach, as described in section 6.5. The signal fraction can be linked to $\langle \sigma_A \nu \rangle$ using the simulated signal through the equation :

$$\langle \sigma_A \nu \rangle = \mu_{90\%}\, N_{bg}\, \frac{2}{T\, A}\, \frac{4\pi m_\chi^2}{J_a(\Psi)\, \phi_\nu} \tag{6.10}$$

The upper limit on $\langle \sigma_A \nu \rangle$ for background events only is then calculated generating a 100 thousands pseudo-experiments sample. The sensitivity corresponds to the median value of the given 90% upper limits.

The code used for the combined analysis is based on the MLSandbox project [**MLSandbox**] for the likelihood method, and can be found in the annex section. Multiple version of this code were made during our analysis, depending on either the IC79 or IC86 data were used. Indeed, the file format was different for these two data selections. In the case of the IC79 selection, i3 files were used, while for the other one, ROOT files were prefered. The code was thus adapted from Python to PyROOT in order to read the new file format.

The analysis method was first conducted on both IceCube and ANTARES data in order to obtain the upper and median limits for each experiments. Once the individual sensitivities were obtained, the combined analysis was performed.

The sensitivity to $\langle \sigma_A \nu \rangle$ for the combined analysis of IceCube and ANTARES is shown in fig. 6.20 to fig. 6.24. In this plots, the blue line is the sensitivity for IceCube, the green one is the sensitivity for ANTARES alone and the red one is the sensitivity obtained by combination of both experiments. For IceCube, the WIMP masses range is extended to masses as low as 10 GeV/c^2, while we are using masses from 50 GeV/c^2 for ANTARES and the combination.

For the $\tau\bar{\tau}$ channel, an improvement of the limit can be seen between 65 and 500 GeV/c^2. Indeed, the combined sensitivity is better than the sensitivities of IceCube and ANTARES alone for that WIMP mass range. A similar improvement can be seen for the $\mu\bar{\mu}$ channel between 50 and 1000 GeV, as well as for the $\nu_\mu\bar{\nu}_\mu$ and W^+W^- channels between 200 and 1000 GeV. However, in the case of the $b\bar{b}$ channel, IceCube dominates the projected sensitivity, as it can be seen in figure 6.21.

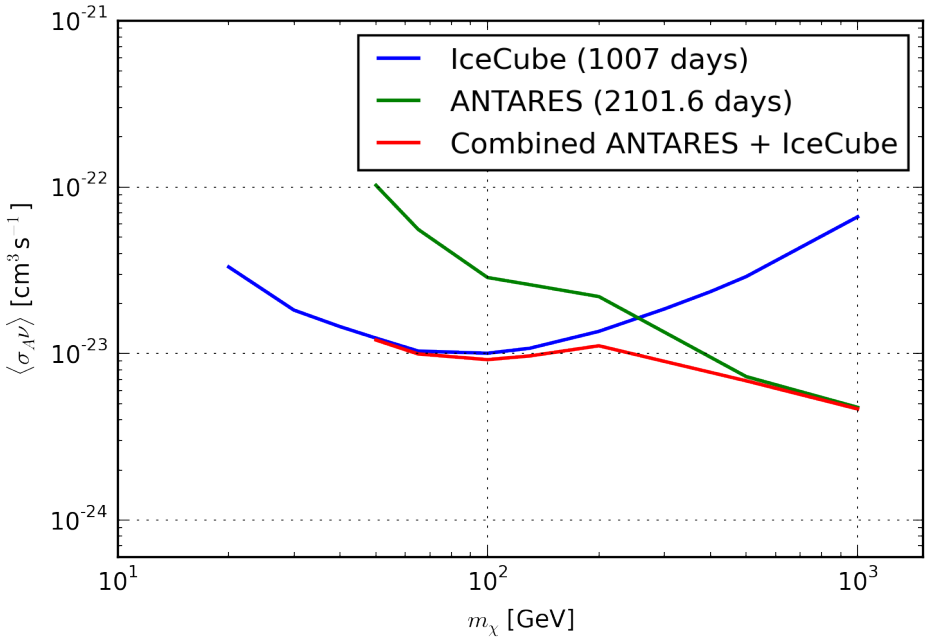

FIGURE 6.20: Sensitivity at 90% C.L of the $\langle \sigma_A \nu \rangle$ as a function of the WIMP mass for IceCube data only (blue), ANTARES data (green) and the combined analysis (red) for the annihilation channel $\chi\chi \leftarrow \tau\bar{\tau}$

1184

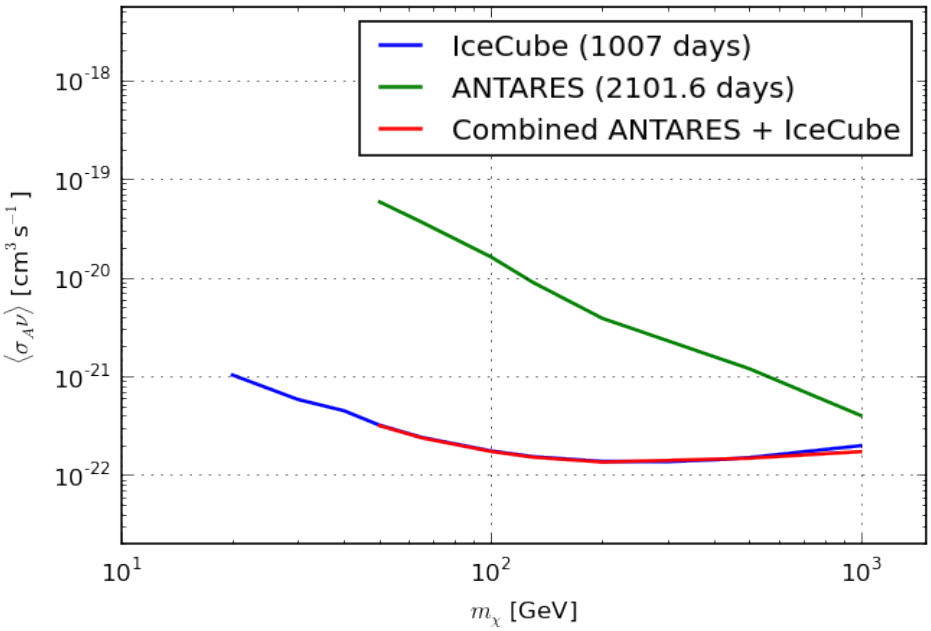

FIGURE 6.21: Sensitivity at 90% C.L of the $\langle \sigma_A \nu \rangle$ as a function of the WIMP mass for IceCube data only (blue), ANTARES data (green) and the combined analysis (red) for the annihilation channel $\chi\chi \leftarrow b\bar{b}$

1185

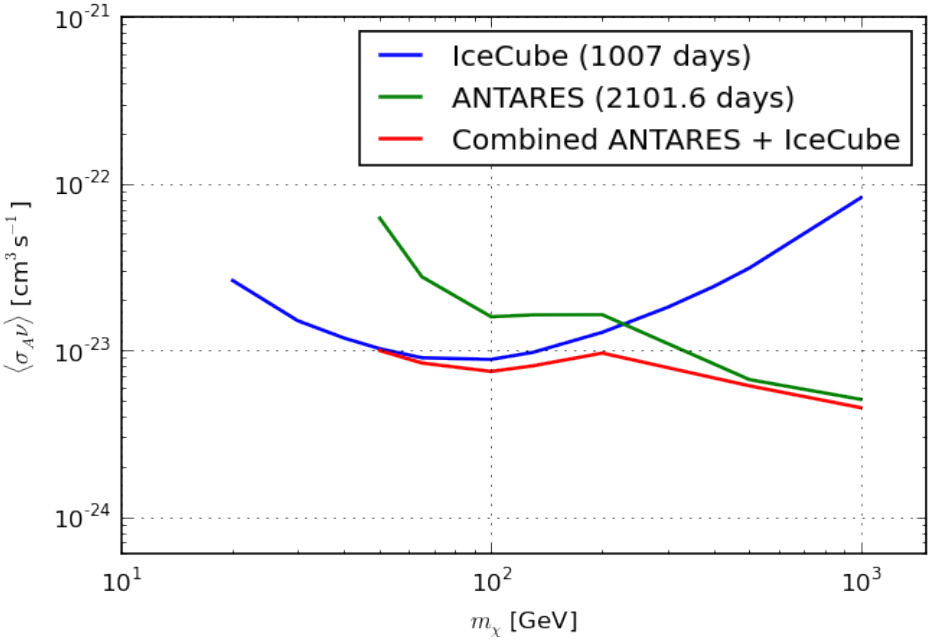

FIGURE 6.22: Sensitivity at 90% C.L of the $\langle \sigma_A \nu \rangle$ as a function of the WIMP mass for IceCube data only (blue), ANTARES data (green) and the combined analysis (red) for the annihilation channel $\chi\chi \leftarrow \mu\bar{\mu}$

1186

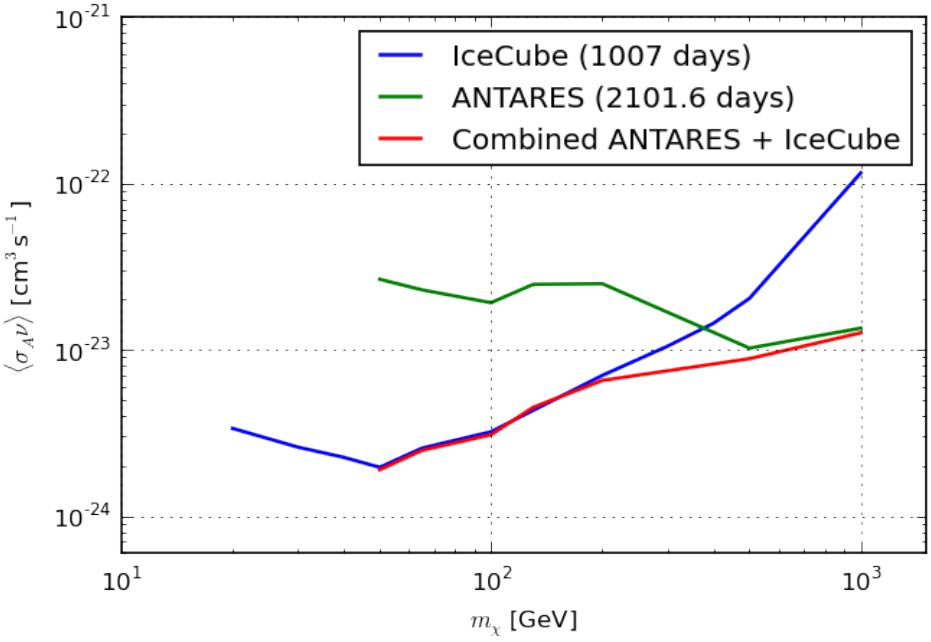

FIGURE 6.23: Sensitivity at 90% C.L of the $\langle \sigma_A \nu \rangle$ as a function of the WIMP mass for IceCube data only (blue), ANTARES data (green) and the combined analysis (red) for the annihilation channel $\chi\chi \leftarrow \nu_\mu \bar{\nu_\mu}$

1187

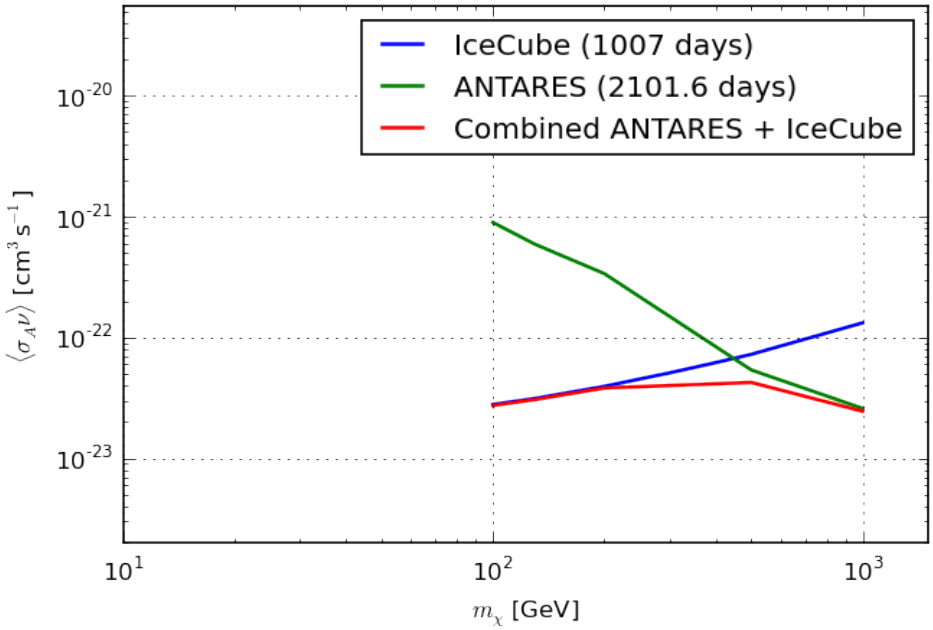

FIGURE 6.24: Sensitivity at 90% C.L of the $\langle \sigma_A \nu \rangle$ as a function of the WIMP mass for IceCube data only (blue), ANTARES data (green) and the combined analysis (red) for the annihilation channel $\chi\chi \leftarrow WW$

1188

Chapter 7

Conclusion

The thermally averaged DM self-annihilation cross-section $\langle \sigma_A \nu \rangle$ was determined for all these WIMP annihilation channels and masses. The combined sensitivity was compared to the IceCube and ANTARES sensitivities alone. An improvement of the sensitivity was observed for the $\tau\bar{\tau}$, $\mu\bar{\mu}$, $\nu_\mu\bar{\nu}_\mu$ and W^+W^- annihilation channels. However, for the $b\bar{b}$ channel, the IceCube component was dominated the combined likelihood, such that, in that case, the combined sensitivity is sensibly the same as the IceCube one.

This analysis opens the way to future combined searches. In the future searches, other annihilation channels and DM halo density profiles could be explored in order to improve the limit on the DM self-annihilation cross-section. More than IceCube and ANTARES, the combination could be extended to other neutrino telescopes such as the ones mentioned in section 2.3.

This analysis could also be improved by considering a different statistical method. This analysis was performed using a *binned* likelihood method, that is to say by using PDFs divided into small "bins". However, this method is not ideal for that kind of analysis. That is the reason why, we would like to pursue this analysis using an *unbinned* likelihood method, which turn out to be more powerful. Also, we could consider specific characteristics of DM in order to sharpen the combined search. Thus, the specific signature of DM in the energy spectrum could be taken into account in future analysis.

List of Abbreviations

AGN	**A**ctive **G**alactic **N**uclei
BDT	**B**oosted **D**ecision **T**ree
B.R.	**B**ranching **R**atio
BSM	**B**ehind **S**tandard **M**odel
C.L.	**C**onfidence **L**evel
CMB	**C**osmic **M**icrowave **B**ackground
CNB	**C**osmic **N**eutrino **B**ackground
COG	**C**entre **O**f **G**ravity
CR	**C**osmic **R**ay
dec	**dec**lination
DIS	**D**eep-**I**nelastic **S**cattering
DOM	**D**igital **O**ptical **M**odule
GC	**G**alactic **C**entre
GRB	**G**amma **R**ay **B**urst
GZK	**G**reisen-**Z**atsepin-**K**uzmin **HE**
High **E**nergy	
HLC	**H**ard **L**ocal **C**oincidence
LCM	**L**ocal **C**ontrol **M**odule
LE	**L**ow **E**nergy
LHC	**L**arge **H**adron **C**ollider
llh	**l**og **l**ikeli**h**ood
LSP	**L**ight **S**USY **G**alactic **P**article
MACHO	**M**assive **A**stronomical **C**ompact **H**alo **O**bject
MoND	**M**odified **N**ewtonian **D**ynamic
NCh	**N**umber of **Ch**annel
$\mathbf{N}_{str}$	**N**umber of **Str**ing
NFW	**N**avarro-**F**renck-**W**hite
NRP	**N**uclear **R**esonance **P**roduction
OM	**O**ptical **M**odule
PDF	**P**robability **D**ensity **F**unction
pe	**p**hoto-**e**lectron
PMT	**P**hoto**M**ultiplier **T**ube
QES	**Q**uasi-**I**nelastic **S**cattering
RA	**R**ight **A**scension
SM	**S**tandard **M**odel
UHECR	**U**ltra-**H**igh **E**nergy **C**osmic **R**ay **WIMP**
Weakly **I**nteracting **M**assive **P**article	

Bibliography

[1] M. Bossa. "DarkSide-50, a background free experiment for dark matter searches". In: *Journal of Instrumentation* 9:C01034 (2014).

[2] P. A. Cherenkov. "Visible Radiation Produced by Electrons Moving in a Medium with Velocities Exceeding that of Light". In: *Physical Revieuw* 52 (1937), 378–379.

[3] J. Mather D. Fixsen. "The Spectral Results of the Far-Infrared Absolute Spectrophotometer Instrument on COBE". In: *Astrophysical Journal* 581 (2) (2002), 817–822.

[4] R. Bernabei et al. (DAMA Collaboration). "Search for WIMP annual modulation signature: Results from DAMA / NaI-3 and DAMA / NaI-4 and the global combined analysis". In: *Phys. Lett.* 480:23 (2000).

[5] R. Bernabei et al. (DAMA/LIBRA Collaboration). "First results from DAMA/LIBRA and the combined results from DAMA". In: *The European Physical Journal* 56:333 (2008).

[6] M. Danninger. "Searches for Dark Matter with IceCube and DeepCore: New constraints on theories predicting dark matter particles". PhD thesis. Stockholm University, 2013, p. 14.

[7] J. de Dios Zornoza and J. Zuniga. "The ANTARES neutrino telescope". Proceedings of the SEA conference. 2012.

[8] P. Salucci F. Nesti. "The Dark Matter Halo of the Milky Way, AD 2013". In: *Journal of Cosmology and Astroparticle Physics* 2013 (2013).

[9] V. Rubin; W.K. Jr Ford and N. Thonnard. "Extended rotation curves of high-luminosity spiral galaxies. IV - Systematic dynamical properties, SA through SC". In: *Astrophysical Journal* 225 (1978), pp. L107–L111.

[10] J. A. Formaggio and G. P. Zeller. "From eV to EeV: Neutrino Cross-Sections Across Energy Scales". In: *Reviews of Modern Physics* 84 (2012), 1307–1341.

[11] M.G.Aartsen et al. (IceCube Collaboration). "Measurement of the South Pole ice transparency with the IceCube LED calibration system". In: *Nucl.Instrum.Meth.* A711 (2013), pp. 73–89.

[12] R. Abbasi et al. (IceCube Collaboration). "Calibration and characterization of the IceCube photomultiplier tube". In: *Nucl.Instrum.Meth.A618* 38 (2010), pp. 139–152.

[13] R. Abbasi et al. (IceCube Collaboration). "The IceCube Data Acquisition System: Signal Capture, Digitization, and Timestamping". In: *ScienceDirect* 601 (3 April 2009).

[14] S.D.M. White J.F.Navarro C.S.Frenck. "The Structure of Cold Dark Matter Halos". In: *Astrophysical Journal* 462(1):536-575 (1996).

[15] C. Kopper. "Performance Studies for the KM3NeT Neutrino Telescope". PhD thesis. Friedrich-Alexander-Universit at Erlangen-Nurnberg, 2010.

[16] V. Kulikovskiy. "Neutrino astrophysics with the ANTARES telescope". PhD thesis. Universita degli Studi di Genova, 2014, p. 15.

[17] D. S. Akerib et al. (the LUX collaboration). "First results from the LUX dark matter experiment at the Sanford Underground Research Facility". In: *Physical Review Letters* 112:091303 (2014).

[18] P. Liu. "A new phase function approximating to mie scattering for radiative transport equations". In: *Physics in Medicine and Biology* 39 (1025 1994).

[19] M. Milgrom. "A Modification of the Newtonian dynamics as a possible alternative to the hidden mass hypothesis". In: *The Astrophysical Journal* 270 (1983), 365–370.

[20] Lars Bastian Mohrmann. "A Measurement of the Energy Spectrum and Flavor Composition of the Cosmic Neutrino Flux Observed with the IceCube Neutrino Observatory". PhD thesis. Humboldt-Universität zu Berlin, 2015, p. 59.

[21] K. Woschnagg P. B. Price and D. Chirkin. "Age vs depth of glacial ice at South Pole. Geophysical Research Letters". In: *Geophysical Research Letters* 27 (2000), 2129–2132.

[22] D. Perkins. *Particles Astrophysics*. 2003, p. 103.

[23] M. Wolf. "Indirect Searches for Dark Matter in the Milky Way with IceCube-DeepCore". PhD thesis. Stockholm University, 2016, pp. 84–86.

[24] C. Andreopoulos et al. "The GENIE Neutrino Monte Carlo Generator: Physics and User Manual". In: *Nucl.Instrum.Meth.* A614 (2010), pp. 87–104.

[25] C. E. Aalseth et al. "Experimental constraints on a dark matter origin for the DAMA annual modulation effect". In: *Physical Review Letters* 101:251301 (2008).

[26] D. Heck et al. "CORSIKA: A Monte Carlo code to simulate extensive air showers". In: *Technik und Umwelt* (1998), p. 98.

[27] E. Armengaud et al. "A search for low-mass WIMPs with EDELWEISS-II heat and ionization detectors". In: *Physics Review D* 86:051701 (2012).

[28] G. Angloher et al. "Results on low mass WIMPs using an upgraded CRESST-II detector". In: *European Physics Journal C* 74(12):3184 (2014).

[29] J. A. Hinton et al. "The Status of the H.E.S.S. project". In: *New Astronomy Reviews* 848:331–337 (2004).

[30] J. Angle et al. "First Results from the XENON10 Dark Matter Experiment at the Gran Sasso National Laboratory". In: *Physical Review Letters* 100:021303 (2008).

[31] J. Holder et al. "Status of the VERITAS Observatory". In: *American Institute of Physics Conference Proceedings* 1085:657 (2008).

[32] K. Choi et al. "Measurement of separate cosmic-ray electron and positron spectra with the Fermi Large Area Telescope". In: *Physical Review Letters* 108:011103 (2012).

[33] K. Choi et al. "Search for neutrinos from annihilation of captured low-mass dark matter particles in the Sun by Super-Kamiokande". In: *Physical Review Letters* 114(14):141301 (2015).

[34] K. Nakamura et al. "Review of particle physics". In: *Journal of Physics G: Nuclear and Particle Physics* 37 (2010).

[35] M. Ackermann et al. "Optical properties of deep glacial ice at the South Pole". In: *JOURNAL OF GEOPHYSICAL RESEARCH* 111 D13203 (2006).

[36] M. Aguilar et al. "First Result from the Alpha Magnetic Spectrometer on the International Space Station: Precision Measurement of the Positron Fraction in Primary Cosmic Rays of 0.5-350 GeV". In: *Physical Review Letters* 110:141102 (2013).

[37] O. Adriani et al. "An anomalous positron abundance in cosmic rays with energies 1.5-100 GeV". In: *Nature* 458:607–609 (2009).

[38] R. Abbasi et al. "The Design and Performance of IceCube DeepCore". In: *Astroparticle Physics* 35 (2012).

[39] Z. Ahmed et al. "Search for Weakly Interacting Massive Particles with the First Five-Tower Data from the Cryogenic Dark Matter Search at the Soudan Underground Laboratory". In: *Physical Review Letters* 102:011301 (2009).